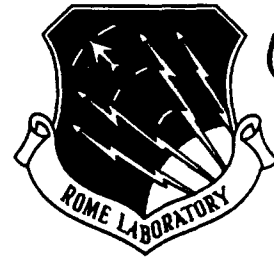RL-TR-91-398
In-House Report
December 1991
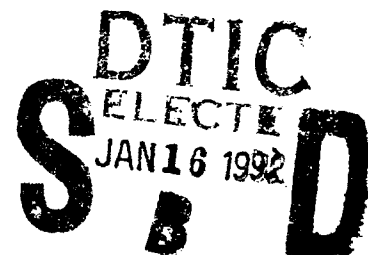
AD-A244 343

TIME-DIVISION OPTICAL INTERCONNECTS FOR LOCAL-AREA AND MICRO-AREA NETWORKS

Mark F. Krol, Raymond K. Boncek, Steven T. Johns,
John L. Stacy

DTIC
ELECT
S JAN16 1992
B D

Rome Laboratory
Air Force Systems Command
Griffiss Air Force Base, NY 13441-5700

92 1 15 003

REPORT DOCUMENTATION PAGE

Public reporting burden for this collection of information is estimated to average 1 hour per response, including the time for reviewing instructions, searching existing data sources, gathering and maintaining the data needed, and completing and reviewing the collection of information. Send comments regarding this burden estimate or any other aspect of this collection of information, including suggestions for reducing this burden, to Washington Headquarters Services, Directorate for information Operations and Reports 1215 Jefferson Davis Highway, Suite 1204, Arlington, VA 22202-4302, and to the Office of Management and Budget, Paperwork Reduction Project (0704-0188), Washington, DC 20503

1. AGENCY USE ONLY (Leave Blank)	2. REPORT DATE	3. REPORT TYPE AND DATES COVERED
	December 1991	In-House Feb 89 – Sep 91

4. TITLE AND SUBTITLE	5. FUNDING NUMBERS
TIME-DIVISION OPTICAL INTERCONNECTS FOR LOCAL-AREA AND MICRO-AREA NETWORKS	PE - 62702F PR - 4600 TA - P2 WU - 01

6. AUTHOR(S)

Mark F. Krol, Raymond K. Boncek, Steven T. Johns, John L. Stacy

7. PERFORMING ORGANIZATION NAME(S) AND ADDRESS(ES)	8. PERFORMING ORGANIZATION REPORT NUMBER
Rome Laboratory (OCPA) Griffiss AFB NY 13441-5700	RL-TR-91-398

9. SPONSORING/MONITORING AGENCY NAME(S) AND ADDRESS(ES)	10. SPONSORING/MONITORING AGENCY REPORT NUMBER
Rome Laboratory (OCPA) Griffiss AFB NY 13441-5700	

11. SUPPLEMENTARY NOTES

Rome Laboratory Project Engineer: Mark F. Krol/OCPA/(315) 330-4456

12a. DISTRIBUTION/AVAILABILITY STATEMENT	12b. DISTRIBUTION CODE
Approved for public release; distribution unlimited.	

13. ABSTRACT (Maximum 200 words)

This report describes the development of an optical Time-Division Multiple-Access (TDMA) interconnect suitable for applications in local-area and micro-area networks. The advantages of using time-division techniques instead of frequency-division, wavelength-division, or code-division techniques in a shared-medium environment are discussed in detail. Furthermore, a detailed description of the TDMA architecture is presented along with various experiments pertaining to the actual components needed to implement the system. Finally, experimental data is presented for an actual optical TDMA test bed. The experimental data demonstrates the feasibility of the architecture, and shows that currently the system has the capability to accommodate up to 50 channels. The bit-error rate per channel was measured to be less than 10^{-9} for pseudo-random bit-sequences.

14. SUBJECT TERMS		15. NUMBER OF PAGES
Time-Division Multiple-Access (TDMA), shared-medium, optical correlation, optical modulation		68
		16. PRICE CODE

17. SECURITY CLASSIFICATION OF REPORT	18. SECURITY CLASSIFICATION OF THIS PAGE	19. SECURITY CLASSIFICATION OF ABSTRACT	20. LIMITATION OF ABSTRACT
UNCLASSIFIED	UNCLASSIFIED	UNCLASSIFIED	U/L

Table of Contents

1. Introduction

The speed of VLSI circuits is limited primarily by the low bandwidth-distance product of electrical interconnects.[1] Furthermore, the integration density of VLSI chips is limited by the small number of electrical pin-outs that can be accommodated on the perimeter of a chip without crosstalk. It is well-known that this electrical I/O bottleneck can be remedied with optical interconnects, which provide immunity from crosstalk and an enormous bandwidth-distance product.[2]

The optical interconnection of N VLSI processors, physically distributed over a very small area (transmission distances <<1km, as in chips or boards) and a local area (transmission distances <1km, as in rooms and buildings) have been referred to as a micro-area networks (μANs)[3-8] and local-area networks (LANs). Though it is possible to construct such a μAN or LAN with point-to-point links by simply providing a dedicated link between each processor and every other processor, the number of links required in such a fully-connected topology would grow quadratically with the number of processors N. If the number of processors is large, then the number of links required for full interconnection $N(N-1)/2$ may be impractical to implement. In addition, not all of the links in a fully connected network can be used simultaneously. If, at a given time, every processor is either transmitting or receiving, then the number of links required is between $N/2$ and $N-1$, and the fraction of un-used links is between $(N-2)/(N-1)$ and $(N-2)/N$. Not only is it impractical to provide full interconnection in a large network, but the resources would not be utilized efficiently.

To increase the efficiency and decrease the complexity of interconnections in a network, fewer links can be provided at the expense of requiring a means of sharing these links. For example, in a partially connected network with a star, bus or ring topology, the number of links grows only linearly with the number of users. To provide connectivity in such a network, switching is required to establish connections as they are needed, and release them when they are no longer needed. Consequently, optical μANs require, in addition to point-to-point fiber-optic links, some form of switching.

3

Switches can be broadly classified into two categories, in terms of how connections are established. Those switches in which the end-to-end network connection is established in advance and maintained during the entire transmission are called "circuit switches." Those switches for which the transmission is segmented into short blocks of data preceded by an address (packets) and piece-wise connections are temporarily established "on the fly" as packets propagate through the network, are called "packet switches." Circuit switches have traditionally been used in telecommunications networks, because the duration of the call is usually much longer than the amount of time required to set up the circuit in advance of a call. Packet switches were developed for data networks in which the traffic is bursty (short transmissions at random intervals) and where the duration of the data burst is not much longer than the amount of time required to set up an end-to-end-circuit. Since it would be inefficient to spend excessive time setting up a dedicated circuit, only to use it for a brief transmission, the connection is established by the packet itself as it propagates. Standards are already being developed for packet-switched networks such as asynchronous transfer mode (ATM) in which the packet comprises 48 bytes of data, and a 5-byte header containing address, priority and error-check information.

Clearly, the potentially large throughput in fiber-optic links, as well as the large number of packets per second, will place severe demands on the required transmission bandwidth and reconfiguration speed of future packet switches for μANs and LANs. Although electronic switching technology has already achieved high switching speeds, it is quite possible that it will be difficult for electronic switches to match the transmission bandwidths that fibers can provide. Of course it is possible to argue that the bandwidth of any individual channel will never exceed the reconfiguration speed or transmission bandwidth of an electronic switch, but many channels are usually multiplexed on the fiber, producing a high aggregate data rate. It is then essential that the transmission bandwidth of the switch match the aggregate bandwidth of the fiber. It is unlikely that this requirement can be met by electronic switches.

Thus photonic switches may be needed to provide a transmission bandwidth that matches the aggregate bandwidth carried by the optical network. If packet switching is used, then the

4

reconfiguration speed of the switch must also be fast. Another advantage of using a photonic switch is that optoelectronic conversion is avoided, which may reduce the cost and increase reliability. Because the photonic switching fabric is transparent to the transmitted optical signal, phase and frequency information are preserved, which may be important in coherent as well as frequency- and wavelength-division multiplexed systems.

Photonic switching architectures can be classified in two categories, interchanger and shared-medium. In the interchanger architecture, switching is performed centrally by a mapping operation. In a space-interchanger (crossbar) switch, signals entering the switch on physically-disjoint input paths are spatially mapped to physically-disjoint output ports. In a time-, wavelength- or frequency-interchanger switch, a set of multiplexed signals on a shared input path are mapped by interchanging time-, wavelength- or frequency-slots. In the shared-medium architecture, a single transmission medium (an optical fiber) is shared by all nodes; a multiaccess protocol performs the switching function. The topology of the shared-medium may be a star, bus, ring or other local area network configuration. Access to the shared-medium may be provided by time-, code-, wavelength- or frequency-division multiple access (T-, C-, W- or FDMA). Access may also be provided by a random access protocol such as carrier sense multiple access with collision detection (CSMA/CD). The task of switching is distributed among the tunable transmitters and/or receivers. Either the shared-medium or the interchanger switch architecture may be used in an optical network. The appropriate choice of architecture will depend, in part, on the insertion loss, maximum the size of N, internal blocking characteristics, required transmission bandwidth and required switching speed. Because the number of processors to be interconnected in an optical network may be very large, and the maximum dimension of interchanger switches can be severely limited by technological considerations, only the shared-medium switch architecture will be considered further below.

We have just seen that optical micro-area and local-area networks can provide flexible communications among VLSI processors and eliminate electrical I/O bottlenecks. In Sec. 2, shared-medium multiple access protocols will be discussed that can avoid the access delays

5

associated with statistical multiple access protocols (which are unacceptable in multiprocessor applications) and increase the throughput, at the expense of wasting optical bandwidth. Time-division multiple access (TDMA, Sec. 2.2c) may be more practical to implement in an optical network than other shared-medium multiple access protocols such as frequency-division (Sec. 2.2a) or code-division (Sec. 2.2b). Since the total throughput of TDMA is given by the inverse of the optical pulsewidth, the throughput can be increased by making the pulse width small. Accomplishing this goal requires avoiding the use of low-bandwidth electronics in the portion of the network that directly processes these short pulses. Instead, optical processing can be used in those portions of the network. The architecture of a TDMA network which uses optical multiple access processing and is self-clocking is described in detail in Sec. 3.1. Experimental demonstrations of key subsystems for optically generating, delaying, modulating and correlating short optical pulses are presented. The feasibility of a variable-integer-delay line which provides rapid tuning, wide tuning range and high precision is demonstrated and described in Sec. 3.2. A transmitter consisting of a mode-locked laser with an external modulator is considered in Sec. 3.3, since arbitrarily short pulses can be controlled with a modulator that need only operate at the bit rate, which translates into extremely high total throughput. The use of an off-chip optical source and an on-chip modulator also has circuit-integration advantages over a laser diode, including lower electrical drive power, electrical drive power that is independent of output optical power, greater ease of hybrid integration on silicon substrates, and less required real-estate on the chip. Experimental measurements of the modulation depth, excess transmission loss and required electrical drive power of an MQW modulator are presented in Sec. 3.3 and related to system performance. In Sec. 3.4, an optical correlation receiver is demonstrated using 2 psec optical pulses and a two-gap photoconductive AND gate. The sensitivity, rise-time and fall-time of the device are measured. In Sec. 4, the demonstration of a 5 Gb/sec optical TDMA network is presented, and its performance is analyzed in Sec. 4.2. Finally, the power budget of the TDMA network is calculated in Sec. 4.3 and it is determined that a 1000-node μAN is feasible.

2. Network access control

2.1 Classical access control methods

When more than one user shares any medium, an access control method is needed to determine when a user is allowed to begin to transmit.[9] Centralized control methods, as the name implies, delegate this decision to a central processor. Though centralized control can guarantee fairness in the decision process, the transmission of control information between the individual users and the control processor may be slow, limiting the total throughput in the network. Also, failure of the central processor will cause the entire network to fail. Distributed control methods, in which each user is responsible for using a protocol that governs access to the shared channel, can avoid some of these problems. Examples of early distributed control methods, developed for copper-based local area networks, include statistical multiple access protocols such as carrier-sense multiple access with collision detection (CSMA/CD) and token passing. Statistical multiple access protocols, as the name implies, only guarantee access to the network on a random basis. Users must contend with one another for access to the network; any given user must wait for the channel to become free before attempting to transmit. With statistical multiple access protocols, the delay in gaining access to the network increases as the number of users attempting to transmit increases. Also, because collisions occur when more than one user attempts to transmit simultaneously, the total throughput on the network decreases as the data rate increases (for a fixed transmission distance and fixed average transmission time). Clearly, statistical multiple access protocols are not suitable for high-data-rate transmission channels such as optical fibers. Furthermore, the access delays associated with statistical multiple access protocols would not be acceptable in many processor interconnect applications, where instantaneous access to network must be guaranteed.

2.2 Multiple access with high throughput and low-delay: shared-medium protocols

To overcome the problems associated with statistical multiple access protocols, another class of distributed protocols, called "shared medium" multiple access protocols, has been developed for fiber-optic networks. Because the capacity of the fiber is so large, shared-medium protocols do not attempt to share the fiber's bandwidth efficiently. In fact, shared medium protocols waste the fiber's bandwidth by dividing the channel into many lower capacity channels, each of which is dedicated to a user. In this way, some of the contention problems inherent in statistical multiple access protocols are avoided. Shared-medium protocols do not utilize the channel as efficiently as do statistical protocols, since each user may only require access to its dedicated channel on a sporadic basis. Therefore, with shared medium multiple access protocols, efficiency of bandwidth utilization is traded for reduced access delay and increased total throughput.

A block diagram of an optical network (μAN or LAN) using a shared-medium multiple access protocol is shown in Fig. 1. A passive star topology is chosen because the number of users (N) allowed can be larger than with other passive network topologies. The network consists of N optical transmitters and N optical receivers on IC chips. Each transmitter consists of a light source producing a unique address signature $s_i(t)$, i=1....N. All address signatures are orthogonal, as defined by the expression

$$\int_0^T s_i(t)s_j(t) \, dt = \begin{cases} 0 & i \neq j \\ 1 & i=j \end{cases} \tag{1}$$

The address signature may be generated by driving the light source directly, by using an external modulator, or internally by the light source itself. Examples of sets of orthogonal address signatures include distinct optical carrier frequencies (or wavelengths), radio-frequency subcarriers, time-hopped code sequences, time slots or spatial positions. We will not consider the

Input Channel 1

$s_1(t)$

L_1 → MOD

data in

Input Channel N

$s_N(t)$

L_N → MOD

data in

Star

$\frac{1}{N}\sum_{i=1}^{N}$

$r(t)$

Output Channel 1

$s_j(t)$

$\otimes$ → $\int_0^T$ → PD_1 → data out

COR

Output Channel N

$s_j(t)$

$\otimes$ → $\int_0^T$ → PD_N → data out

COR

L   = light source
$s_i(t)$ = address signature
MOD = modulator
r(t) = received signal
COR = correlator
PD = photdetector

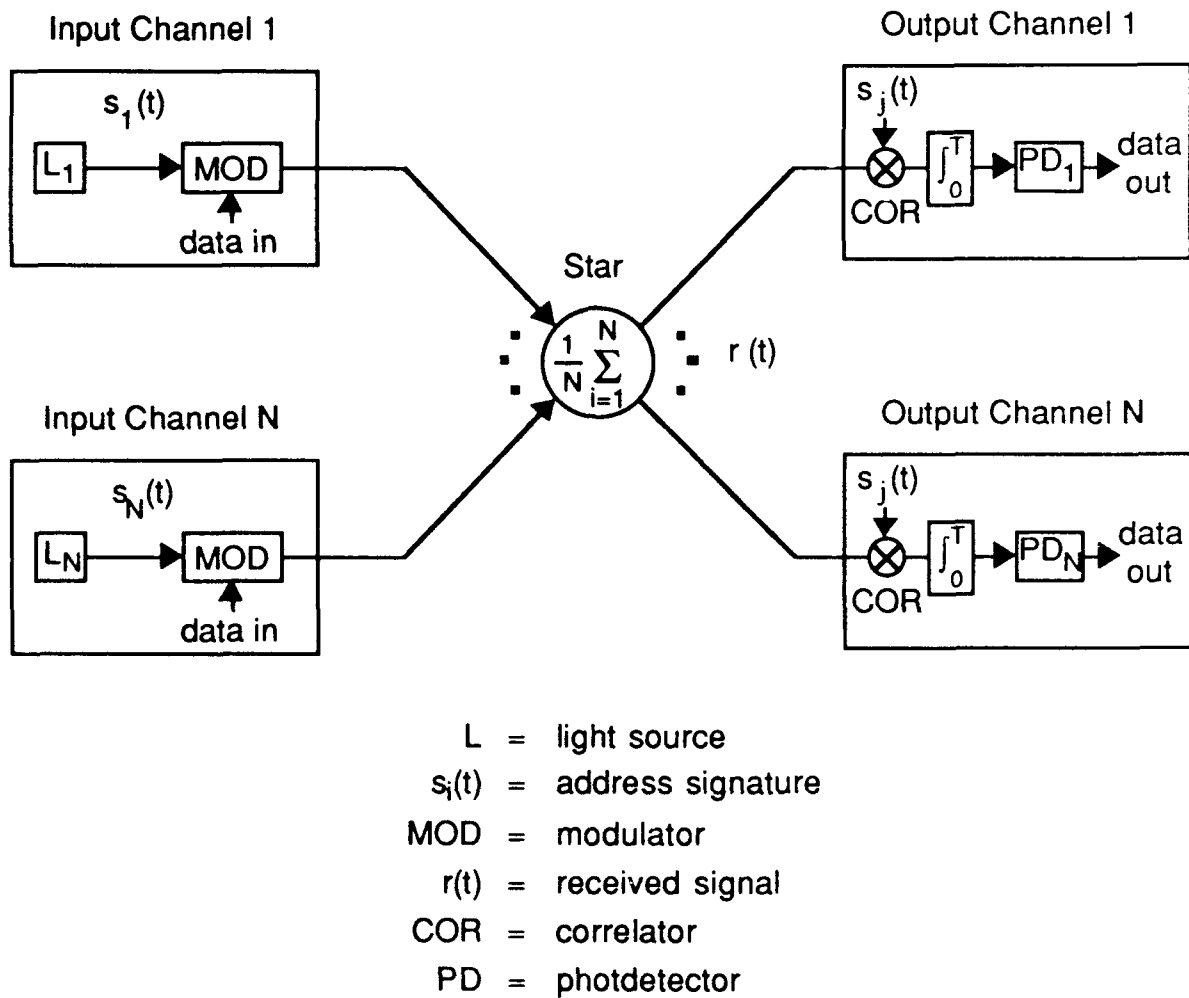**Figure 1** Shared-medium multiple-access optical star architecture.

9

last example further here, since it corresponds to an NxN photonic switch (an active star), which is limited in size to about N=20 with present technology. The address signature is then modulated by a data stream. This modulation can take place either by driving the light source directly or by using an external modulator. In the system shown, the light source internally generates the address signature which is then externally modulated by a data stream. The modulated address signatures are combined by a passive star coupler and uniformly broadcast to all receivers. At any receiver, to tune to the jth transmitter, the received signal r(t) is correlated with the address signature $s_j(t)$ by performing the operation

$$\int_0^T r(t)s_j(t)\, dt \tag{2}$$

Note that the signature inserted at the receiver must be precisely in phase (coherent) with the corresponding signature portion of the received signal. The output of the correlator is then detected and compared to a threshold to recover the data from the jth transmitter. Though the correlation process can be performed electronically after photodetection (as in the case of radio-frequency subcarrier multiple access), the correlation in Fig.1 is performed optically before photodetection. As will be discussed later, with shared-medium multiple access the number of address signatures (the size of the network) increases with the channel bandwidth used. Thus the use of an optical correlator, which has higher bandwidth than an electronic correlator, allows the size of the network to be larger.

Note that the network considered here assigns fixed address signatures to transmitters, and therefore can perform broadcasting. To establish communication, a (tunable) receiver must first poll all transmitters to identify an incoming transmission. To avoid the need for polling, fixed address signatures could be assigned to receivers, and communication would then be established by simply tuning the transmitter to the desired receiver address. However, the fixed receiver

assignment scheme requires a reservation protocol to avoid collisions (*i.e.*, multiple simultaneous transmissions to the same receiver), which may be difficult to implement.

Particular examples of shared medium multiple access protocols which may be used in the optical network shown in Fig.1 include frequency division multiple access (FDMA), code division multiple access (CDMA) and time division multiple access (TDMA). These are illustrated in Fig. 2.

2.2a FDMA

In the first example illustrated in Fig. 2, FDMA, the orthogonal address signatures are given by $s_i(t) \propto \cos\omega_i t$, i=1,...N, corresponding to N distinct carrier frequencies.[10] If the transmitted data has baseband bandwidth 1/T, then the power spectral density $R(\omega)$ of the received signal corresponds to a set of shifted versions of the baseband spectra, centered around the carrier frequencies ω_i, i=1,...N. These spectra must be separated by a guard band of sufficient width to prevent interchannel crosstalk. Optical correlation is performed at the receiver by mixing the received signal with the output of an optical local oscillator. FDMA systems therefore require N laser sources with N selected stable (temperature controlled) center frequencies and narrow linewidths (e.g., DFB lasers), as well as laser local oscillators with stable center frequency, narrow linewidth, wide tuning range and rapid tunability. In addition, some form of frequency registration is needed to establish a common frequency reference throughout the network. The baseband bandwidth required in the transmitter and receiver circuitry is 1/T, and the total spectral bandwidth required in the optical fiber is at least N/T. In addition to the technological problems presently associated with the integration of laser diodes of specified frequencies on IC substrates, the integration of tunable local oscillators and coherent mixers is even a more difficult task. If instead the laser sources and local oscillators are isolated from the IC chip, then modulators with frequency-independent absorption must be integrated on the chip. Another option, which relaxes the stringent linewidth and frequency stability constraints, and avoids the use of coherent local

Frequency Division Multiple Access

$s_i \propto \cos \omega_i t$

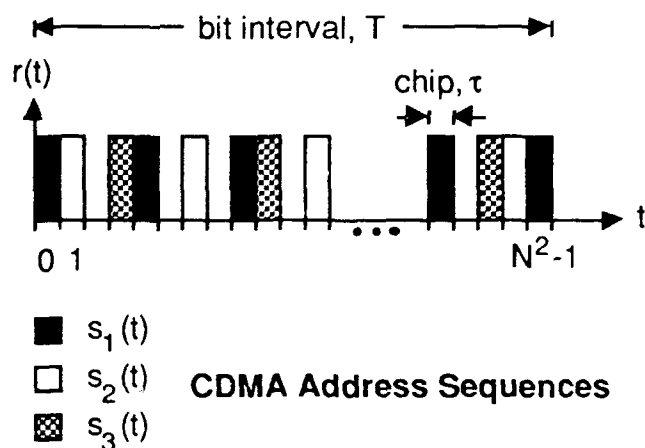correlate r(t) with local oscillator

$R = \mathcal{F}\{r(t)\}$
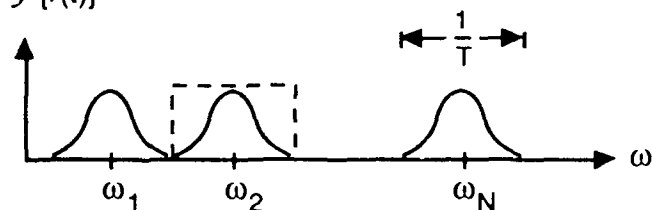
FDMA Spectrum

Code Division Multiple Access

$s_i(t) \propto i^{th}$ address sequence

correlate r(t) with stored sequence
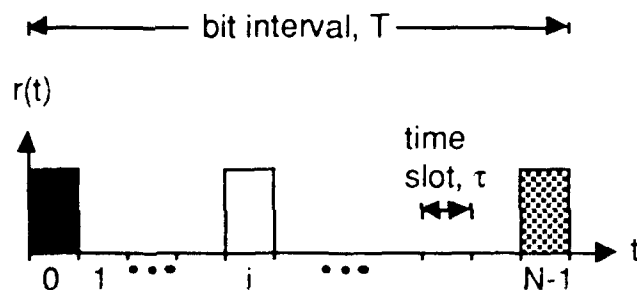

■ $s_1(t)$
□ $s_2(t)$ **CDMA Address Sequences**
▧ $s_3(t)$

Time Division Multiple Access

$s_i(t) \propto u[t-it] - u[t-(i+1)t]$

correlate r(t) with pulse in i_{th} slot

TDMA Frame

Figure 2   Shared-medium multiple-access protocols.

1 2

oscillators, is to widely separate the carrier frequencies ($\omega_{i+1}-\omega_i \gg 1/T$, for $i=1,...N-1$, as in wavelength division multiple access or WDMA[11, 12]), and use a tunable bandpass filter with direct detection at the receiver. Though the most of the above FDMA constraints are relaxed they are nevertheless present in WDMA, and the required tuning range of the receiver is increased as well. For these reasons, it appears that it will be difficult to implement FDMA or WDMA in an optical μAN or LAN.

2.2b CDMA

In the second example illustrated in Fig. 2, CDMA, the orthogonal address signatures correspond to a set of intensity-modulated waveforms $s_i(t)$, $i=1,...N$, of duration T (the bit interval). Each waveform represents a code sequence, which in the case of prime code sequences[13-16] for example, consists of N^2 chips of duration $\tau = T/N^2$. Optical generation and correlation of code sequences using fiber-optic delay lines permits the duration of τ to be very short and the number of code sequences to be large, as has been previously demonstrated.[13-16] For prime code sequences the baseband bandwidth required in the transmitter and receiver is N^2/T (though the use of optical code sequence generation and correlation techniques can reduce the bandwidth required in the optical source and detector to $1/T$), and the total spectral bandwidth required in the optical fiber is also N^2/T. Thus, CDMA requires an extremely large expansion of the channel bandwidth, and a similar increase in transmitter and receiver bandwidth unless optical coding and correlation is used. One advantage of CDMA is that like FDMA it allows asynchronous access to network.

2.2c TDMA

The third example illustrated in Fig. 2, TDMA, is a special case of CDMA, where the orthogonal address signatures are again given by a set of intensity-modulated waveforms $s_i(t)$,

i=1,...N, of duration T (the bit interval). Each waveform represents a code sequence, which in the case of TDMA consists of a single pulse in one of the N chip positions (called time slots) of duration $\tau=T/N$. In the case of fixed-transmitter assignment TDMA, the address signature $s_i(t)$ of the ith transmitter consists of a single pulse in the ith time slot. The receiver correlates the received TDMA frame, consisting of the time-interleaved data streams from all N transmitters, with the address signature of the desired transmitted data. Note once again that the signature inserted at the receiver must be precisely in phase with the corresponding signature portion of the received signal. Therefore, not only does TDMA require phase synchronization throughout the network, but it also requires narrow pulse generation and modulation, time-delays with rapid tuning, wide tuning range and high precision, and high-speed correlation at the receiver. The baseband bandwidth required in the transmitter and receiver circuitry is N/T (though, as discussed below, this constraint is reduced to 1/T if optical encoding and correlation is used), and the total spectral bandwidth required in the optical fiber is also N/T. Thus the baseband and spectral bandwidth requirements of TDMA are a factor N smaller than CDMA, at the expense of requiring network phase synchronization. Since the total throughput of the network with TDMA is $N/T=1/\tau$ (N channels of baseband bandwidth 1/T), the throughput can be increased by making τ small. The architecture of a TDMA network with extremely high throughput will be described below. The experimental demonstration of subsystems for generating, modulating, delaying, synchronizing and correlating optical pulses of very short duration τ will be presented, as well as the the demonstration of the full network architecture at 5Gb/sec.

3. High-throughput networks with optically-processed TDMA

3.1 Optical TDMA network architecture

A fiber-optic network using TDMA can achieve extremely high total network throughput if τ is made very short. Accomplishing this goal requires avoiding the use of low-bandwidth

electronics in the portion of the network that directly processes these short pulses. Instead, optical processing can be used in those portions of the network.[17,18]

The architecture of a TDMA network with dimension (N-1)xN is shown in Fig. 3. In this system, optical processing is used for multiple access. A train of optical clock pulses of duration τ, energy E_L and repetition rate 1/T is generated by a mode-locked laser. To increase the total pulse energy, an array of N synchronous mode-locked lasers may be used instead of a single laser. Using fiber-grating pulse compression techniques, subpicosecond optical pulses can routinely be produced, resulting in a total network throughput of greater than one THz. With fixed transmitter assignment TDMA, the clock period T is divided into a time frame comprised of $N=T/\tau$ time slots, where the ith slot in the frame corresponds to the ith transmitter address. The system shown in Fig. 3 is designed to be self-clocking, so the 0th slot is always reserved for a framing pulse. The output of the pulse compressor is distributed by a 1xN splitter to N-1 fixed optical delays $i\tau$, i=1,...,N-1; the remaining output of the splitter is connected directly to the star coupler and provides a framing pulse for synchronization. The fixed optical delay $i\tau$ moves the optical clock pulse into the ith time slot, yielding a waveform that corresponds to the ith address signature, which is then input to the ith electrooptic modulator integrated on an IC chip. The modulator is driven by an electrical data stream of rate 1/T that modulates the address signature. In this way, arbitrarily short optical pulses can be modulated and the bandwidth of the modulator need only be as large as the baseband bandwidth of the data. As will be discussed below in detail, modulators offer circuit-integration advantages over laser diodes, but suffer a system performance penalty due to their typically lower modulation depth. The modulated address signatures from all N-1 transmitters and the framing pulse are combined in the star coupler and evenly distributed to the receivers on N chips. To maintain timing synchronization throughout the network it is important that all optical path lengths between the pulse compressor output and the receivers, except for intentional address signature delays, be an integral multiple of T, with an error of less than 0.1τ. The TDMA frame comprised of the superposed N-1 modulated address signatures and the framing pulse is illustrated in Fig. 3. Because the framing pulse has bypassed the insertion loss of the
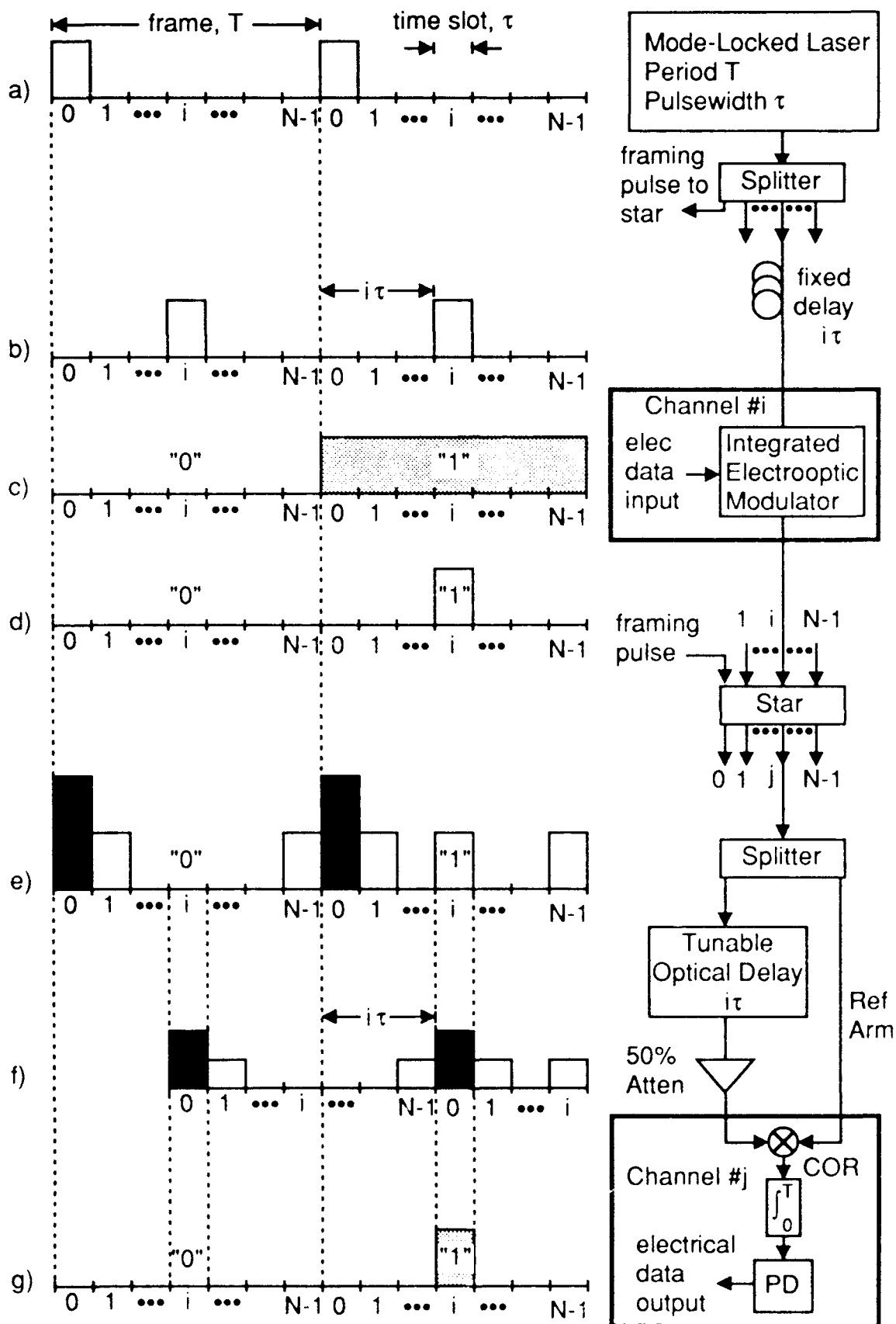
Figure 3 Optical TDMA network architecture.

16

modulator, its amplitude is assumed to be at least 3 dB greater than the modulated address signatures. At each correlation receiver, the TDMA frame is divided by a 1x2 splitter. One arm of the splitter carries a reference version of the TDMA frame. To sample the ith slot of the reference TDMA frame, the other output of the splitter is delayed by iτ with respect to the reference TDMA frame, so that the framing pulse is in phase with the ith slot in the reference TDMA frame. In order to tune the receiver to any one of the time slots, a variable optical time-delay is required. To select among a large number of time slots, the variable time-delay must have wide tuning range and high precision. For rapid access to desired channels, the variable time-delay must also be tunable at high speed. The demonstration of a tunable optical time-delay with these characteristics will be described in detail below. The output of the tunable delay is attenuated by 3 dB, so that the amplitude of the data falls below a specified threshold level, whereas the amplitude of the framing pulse exceeds the threshold. The framing pulse can then be used to carry out self-clocked optical correlation of the ith slot in the reference TDMA frame. Because τ is small, the optical correlation must be performed at high-speed. Though high-speed optical correlation is difficult to do with low-energy pulses, promising experimental results using a photoconductive 'AND' gate will be presented below, as well as the development of an experimental 5 Gb/s optical TDMA network and calculated bit error rate results. First the demonstration of a tunable optical delay line and performance measurements of an integrated modulator will be described.

3.2 Variable-integer-delay line demonstration

A variable-integer-delay line implementation for the optical TDMA coder, shown in Fig. 4, allows a large number of delays with fast reconfiguration time. The feed-forward structure consists of $\log_2 N$ delay stages k=1,..., $\log_2 N$ and an output stage. Thompson has shown analytically that a feed-forward structure requires fewer stages than a feed-back structure[19]. Each delay stage consists of a 2x2 optical switch, a connection to the next stage at one output, and a fixed optical delay in excess of the "connection" delay at the other output. The value of the fixed
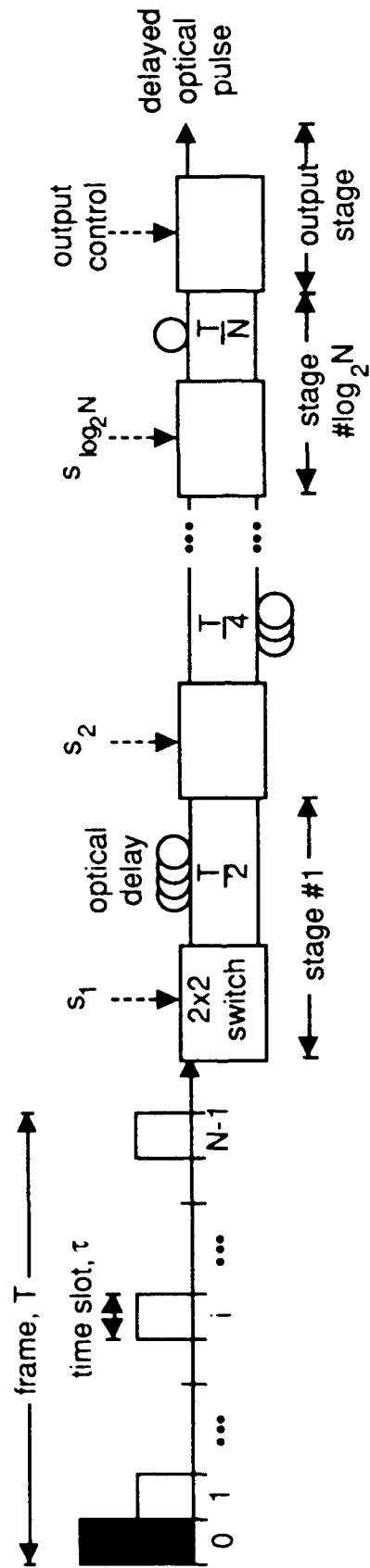
1 7

Figure 4 Variable-integer-delay line optical TDMA coder.

excess delay for the kth stage is $T/2^k$. Only one input to the first stage is used. The output stage consists of a 2x2 optical switch, where only one output is used. Each optical switch can be set in either the bar or the cross state. The state of a switch is set by the electrical control input, where a 0 at the control sets the 2x2 switch in the cross state, whereas a 1 sets the 2x2 switch in the bar state.

The state of the coder is set by a control sequence $(s_1, s_2, ..., s_{logN})$, where control bit s_k sets the state of the kth stage, and the output stage is set equal to 0 if the parity of the control sequence is odd, or to 1 if the parity of the control sequence is even. The output stage serves only to ensure that the delayed pulse always exits at the chosen output of the 2x2 optical switch. The control sequence for the jth slot is generated from the binary representation of the integer j, $(b_1, b_2, ..., b_{logN}$, where b_1 is the most significant bit, according to the rule $s_1=\{$the complement of $b_1\}$, and for $i= 2, ..., log_2N$, $s_i= 0$ if $b_i=b_{i-1}$, otherwise $s_i=1$. After the control sequence has set the coder, the sampled data will be delayed by an amount $j\tau$ in excess of the reference delays, accomplishing the desired time-division encoding operation.

An experimental demonstration of an optical TDMA variable-integer-delay line coder is presented for 64 100 Mbit/sec channels.[20] Here T=10 nsec and τ=156.25 psec. The complete coder requires six delay stages k=1,...,6 with time delays $D_k=10/2^k$ nsec, corresponding to fiber lengths $L_k=2.052/2^k$ m, where the index of refraction of the fiber core is n_f=1.462. If the error in time delay is required to be less than 10% of a time slot, then the aggregate positioning error must be less than 3.2 mm, or 0.53 mm per stage, requiring careful trimming of the fiber lengths.

In this demonstration, only stages #1, 2 and 6 are implemented, demonstrating the longest D_1=5 nsec), intermediate (D_2=2.5 nsec), and shortest (D_6=156.25 psec) delays, and allowing access to eight times slots: 0,1,16,17,32,33,48,49. The experimental setup of the coder, comprised of three LiNbO$_3$ polarization independent directional couplers (DC) with 50 MHz bandwidth and one passive coupler (C1) interconnected by single mode fiber (SMF) delays, is shown in Fig. 5. Use of a passive coupler at the output stage, rather than another directional coupler, introduces 3dB of additional loss. The fiber delays were trimmed by carefully measuring
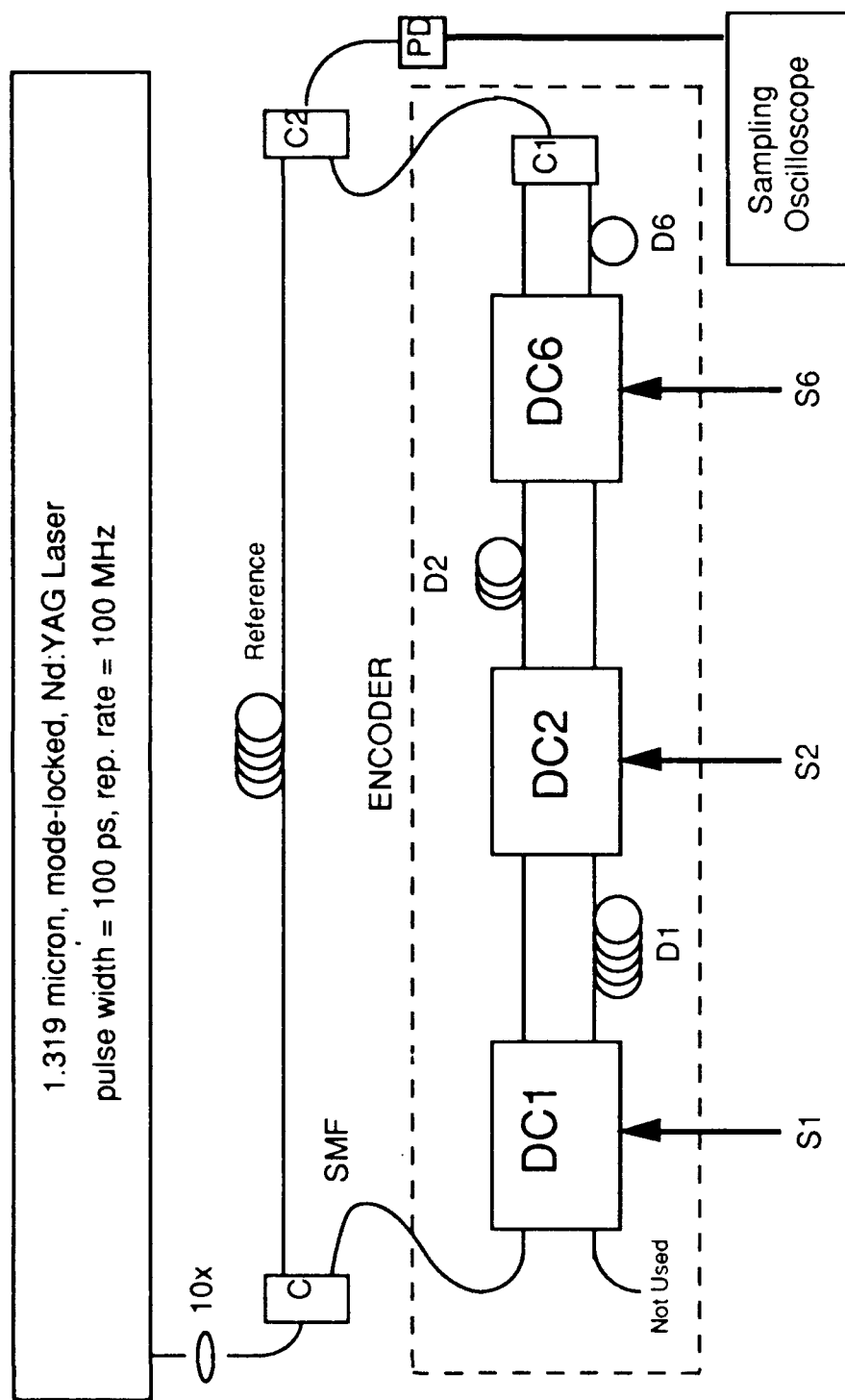
Figure 5 Experimental setup for an eight channel coder demonstration.

and cutting the required lengths. Low-loss connections between the fiber delays and the DC pigtails were made using a fusion splicer. The state of the coder is set by applying a bias voltage of zero volts (cross state) or 20 volts (bar state) to each of the directional couplers. The reconfiguration time of the coder is determined by the switching speed of the directional couplers.

The various delays produced by the coder were measured using 1.3 μm wavelength 100 psec optical pulses generated by a mode-locked Nd:YAG laser with 100 MHz repetition rate. As shown in Fig. 5, the output of the laser is split by coupler (C) so that part of the optical pulse propagates through the coder and the remainder through a reference delay. The output of the coder and the reference delay are combined by a coupler (C2), detected by a 20 GHz-bandwidth photodetector (PD) and displayed on a sampling oscilloscope.

Shown in Fig. 6 are the reference pulses (higher peaks) and encoded pulses (lower peaks), corresponding to the following time slots: (a) slot 0 (ideal delay 0 nsec); (b) slot 1 (ideal delay 156.25 psec); (c) slot 16 (ideal delay 2.5 nsec); (d) slot 32 (ideal delay 5 nsec); (e) slot 49 (ideal delay 7.65625 nsec). Slots 17, 33 and 48 were also encoded but the results are not shown here. The time delay relative to slot 0, measured with the oscilloscope's cursor function, is shown for each case. The maximum aggregate error in measured delay is 2.5% of a time slot. This could be due to measurement error (positioning of the cursor on the oscilloscope) or an error in the length of fiber in stage #2.

The measured input and output powers of the coder are 399 μW and 1 μW, corresponding to approximately 26 dB total insertion loss. This includes 3 dB splitting loss in C1, and insertion losses of 3.5 dB in DC1, 4.5 dB in DC2 and 15 dB in DC6. These insertion losses are primarily due to fiber-to-waveguide coupling at the input and output of the directional couplers.

In general, the most suitable technology for implementing the optical TDMA coder is determined by the number of channels N and the bit rate per channel 1/T: T/2 determines the maximum delay required, whereas T/N determines the minimum delay as well as the precision required. For delays T/2 longer than approximately 50 ps (1/T<10 Gbit/sec), fiber-optic delays are suitable due to the long path length required (> 1 cm). For delays shorter than 50 ps, integrated-
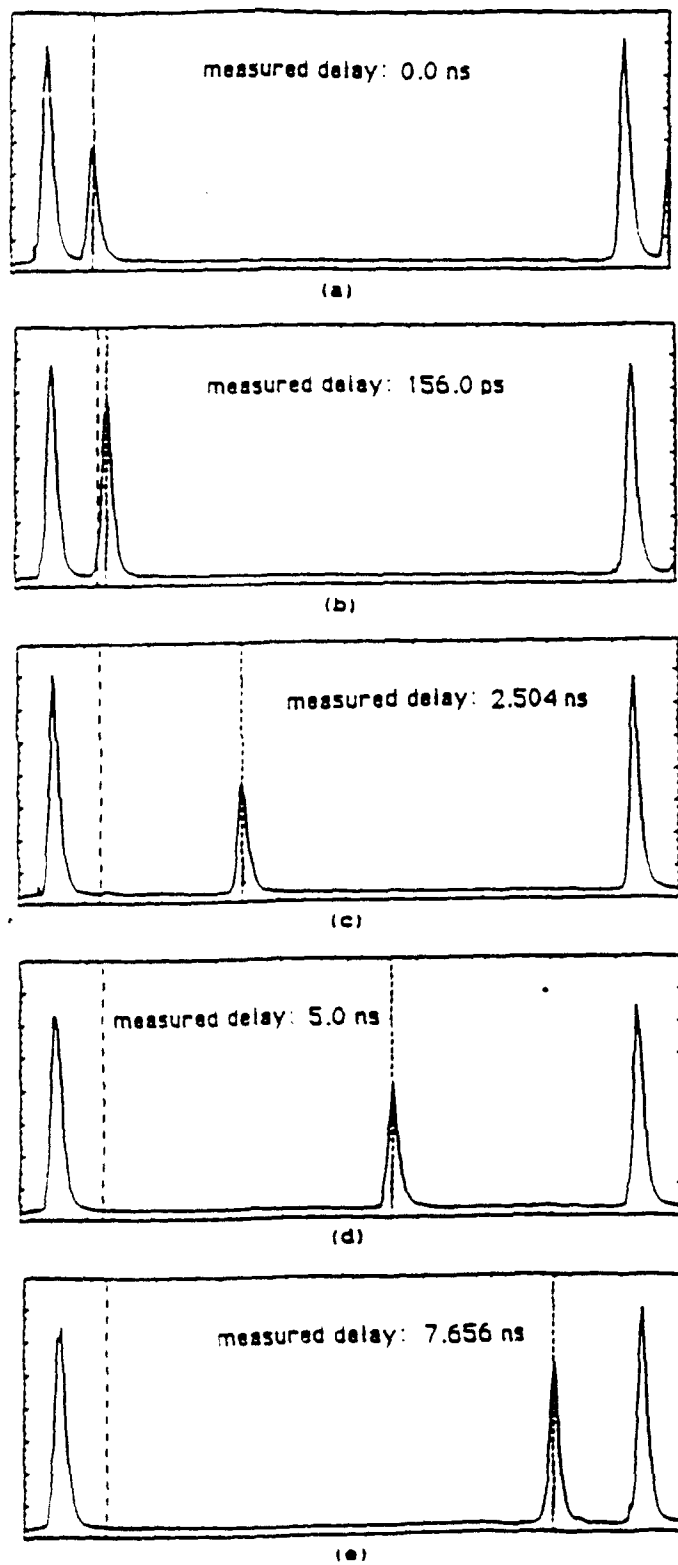
2 1

Figure 6 Measured delays generated with the eight channel coder.

optic waveguides are suitable, since lithographic techniques can routinely yield a precision of less than 1 μm (5 fsec delay).

In situations where N is large, both long and short delays, using fibers and integrated-optics, may be required. Here the main difficulty would be in trimming the fiber length with an error of less than, say, T/10N. For example, if 1/T=1 Gbit/sec and N=1,000 (10 stages) then the total error in delay should be less than 20 μm. This is easily achieved with integrated-optic waveguides, which would be used for the last seven stages of the coder, ranging in length from 1.25 cm (T/16) to 195 μm (T/1028). However, this precision could not easily be achieved with fiber-optic delays, which would be used for the first three stages of the coder, ranging in length from 10 cm (T/2) to 2.5 cm (T/8). A small static adjustment in the fiber length could be made, for example, by stretching the fiber at high temperature.

The maximum number of stages $\log_2 N$ that can be used is limited by the insertion loss. The insertion loss can be minimized in the integrated-optic delay stages by integrating all of the stages together, including the directional couplers and the waveguide delays, on a single substrate. The insertion loss in the fiber-optic delay stages can be compensated using optical amplifiers. In this way, the implementation of an optical TDMA coder capable of addressing 1000 one Gbit/sec channels with subnanosecond reconfiguration time may be feasible.

3.3 Integrated-modulator/ transmitter

The main reason a mode-locked laser with an external modulator is used in Fig. 3 is that we can modulate arbitrarily short optical pulses (τ<1 ps) with a modulator that need only operate at the bit rate 1/T, which in turn provides extremely high throughput 1/τ in the TDMA network. Note that to increase the pulse energy arriving at each modulator a synchronous array of N mode-locked lasers may be used instead of a single laser.

The use of an off-chip optical source and on-chip modulator also has other advantages compared to an on-chip laser diode from the perspective of circuit integration. These advantages

23

include lower electrical drive power, electrical drive power that is independent of output optical power, greater ease of hybrid integration on silicon substrates, and occupying far less real estate on the chip. Clearly the electrical drive power required should be compatible with the other devices on the chip, and the ease of hybrid integration will influence the compatibility these devices with existing silicon integrated circuit technology. For this reason, integrated modulators, particularly of the multiple quantum well type, have received considerable attention in recent years. A notable example is the demonstration of a GaAs-AlGaAs multiple quantum well (MQW) modulator grown on a silicon substrate.[21]

Experimental measurements were made of the modulation depth, excess transmission loss and required electrical drive power, to evaluate the performance of an MQW modulator in the system shown in Fig.3. The experimental setup is shown in Fig. 7. The modulator consists of a p-i-n diode in which the intrinsic layer is an MQW composed of sixty 140 Å thick GaAs quantum wells separated by 160 Å thick $Al_{0.3}Ga_{0.7}As$ barriers.[22,23] When a reverse voltage is applied to the diode, the band edge of the MQW shifts toward lower energy, and the exciton absorption peak flattens. These effects change the optical absorption. If the wavelength of the optical signal lies just above the band edge, a small change in applied reverse voltage can result in a large change in transmitted light.

In Fig.8, the photocurrent is shown as a function of wavelength for bias voltages of 0, 2, 6 and 10 volts. As the bias voltage is increased, the absorption edge shifts to longer wavelengths as expected. The n=1 heavy hole and n=1 light hole exciton peaks are both clearly visible near the absorption edge. Periodic variations of the photocurrent with wavelength are due to residual Fabry-Perot interference effects. The additional peak near $\lambda=0.825$ μm for large bias voltage is evidence of the formerly forbidden n=2 heavy hole to n=1 electron transition.

The normalized photocurrent is shown as a function of applied voltage in Fig.9 for $\lambda=0.8597$ μm and for $\lambda=0.8583$ μm. If the modulation depth β is defined in terms of the transmitted optical power P as
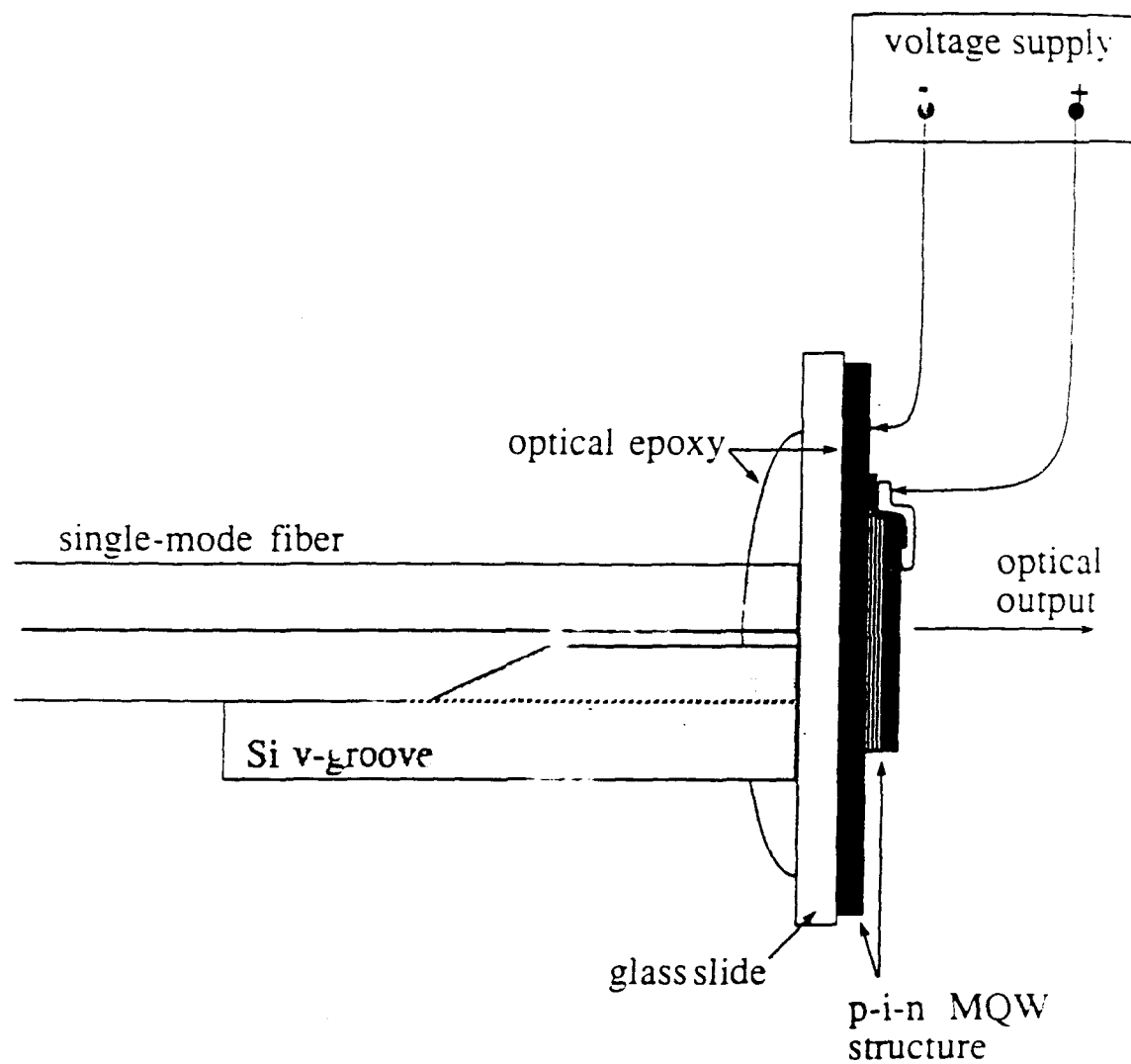
Figure 7   Experimental setup to measure modulation depth, excess transmission loss, and required electrical drive power of a multiple quantum well modulator.
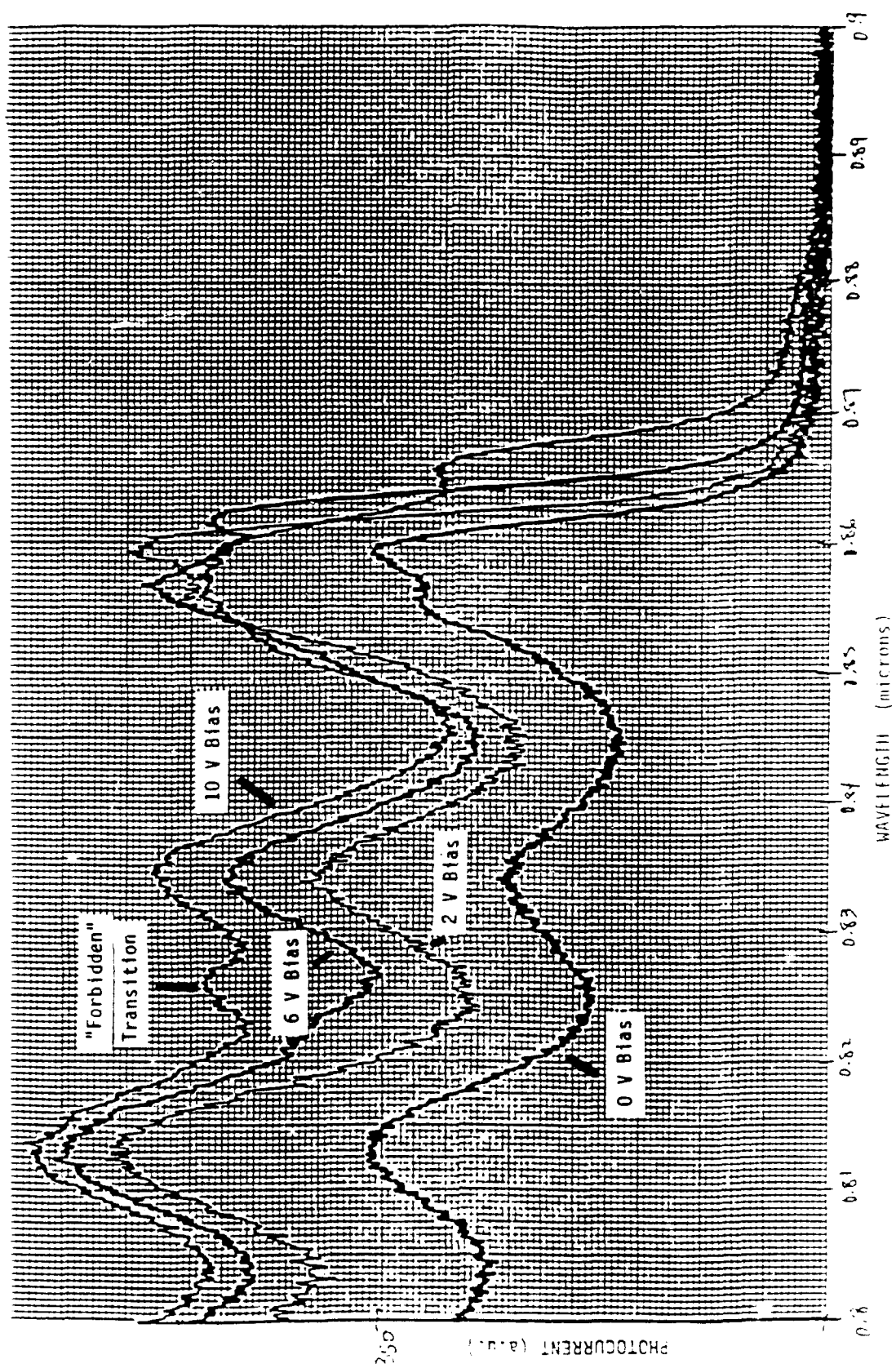
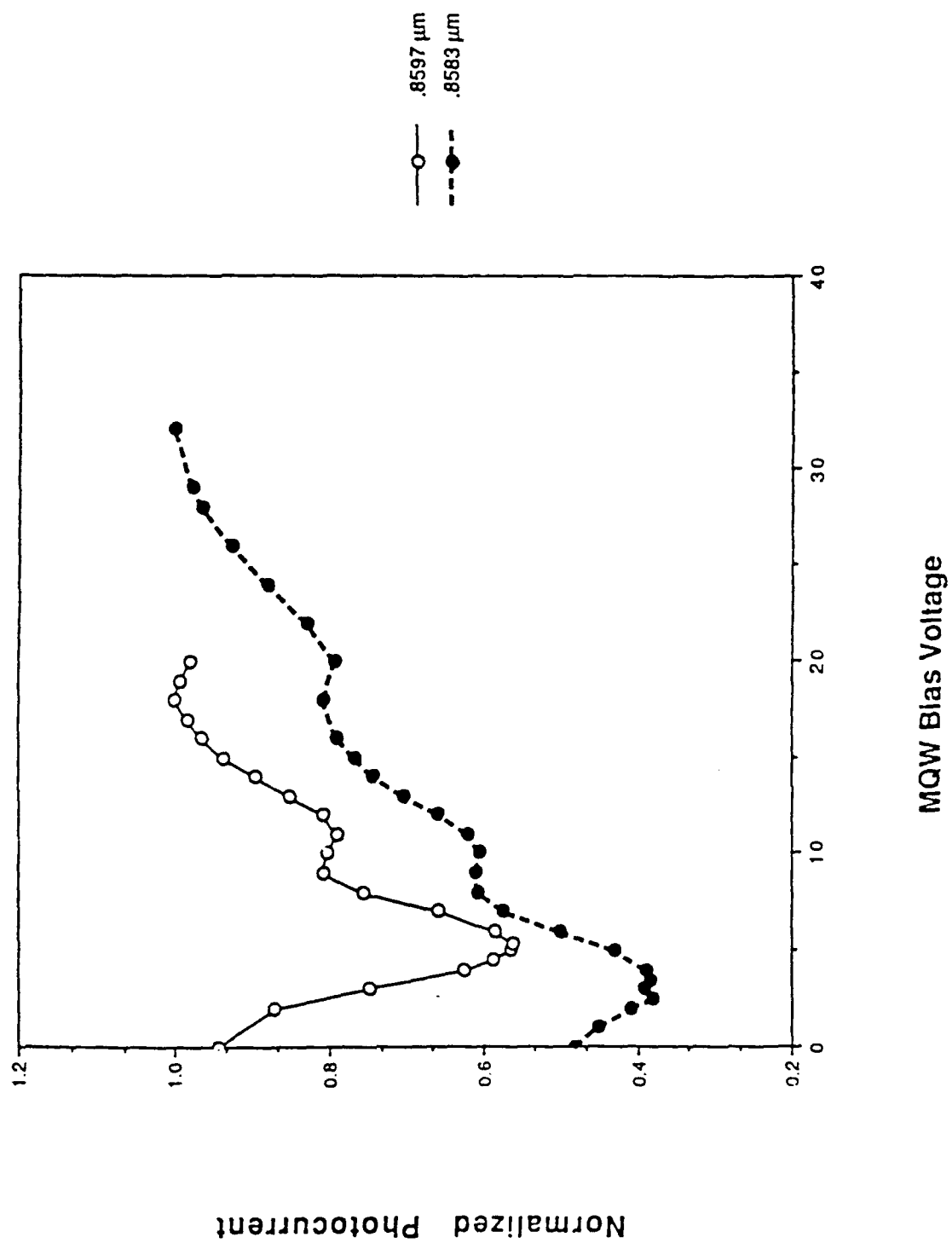**Figure 8** Measured photocurrent spectra of the GaAs/AlGaAs MQW modulator.

26

Figure 9 Measured photocurrent as a function of bias voltage for wavelengths of 859.7 nm and 858.3 nm.

27

$$\beta = \frac{P_{max} - P_{min}}{P_{max}}, \tag{3}$$

then the maximum value of the modulation depth is $\beta=0.5$, obtained for $\lambda=0.8597$ μm and a bias voltage swing from $V_{min}=0$ volts to $V_{max}=5$ volts. The sharp absorption edge in MQW devices is essential in achieving high modulation depths with low bias voltages, but also accounts for the extreme wavelength sensitivity of MQW modulators. For example, as seen in Fig.9, if the input light is detuned from the optimum wavelength by only 1.4 nm (i.e., $\lambda=0.8583$ μm), the modulation depth is reduced substantially. The non-unity depth of the modulator results in a power penalty, which in turn can degrade the performance of the system, as will be discussed below.

The excess transmission loss of the modulator was measured to be 2.2 dB, which is caused primarily by Fresnel reflections due to index of refraction mismatch at the glass-GaAs and GaAs-air interfaces.[24] If a single mode fiber were used rather than power meter to collect the light exiting the modulator, the excess loss might exceed 2.2 dB. In the analysis below, we will assume that the total excess loss in this case is about 3 dB.

The average electrical drive power of the modulator is given by

$$<P_{electrical\ drive}> = \frac{\omega C}{2} (V_{min}^2 - V_{max}^2) \tag{4}$$

where ω is the modulation frequency, C is the capacitance of the modulator, and the input electrical data stream is comprised of equiprobable 0 and 1 bits. The capacitance of the modulator was measured to be 20 pF when no light was applied and would be slightly higher with reverse bias applied and light absorbed[24]. However the device tested had a large surface area (0.2 mm^2). Since the area of the device needs to be only slightly larger than the 16 μm^2 of a single-mode fiber core (say 20 μm^2), the capacitance could be scaled down to approximately C=2 fF. The average electrical drive power of a 20 μm^2 area device is shown in Fig.10 for modulation frequencies $\omega=5$
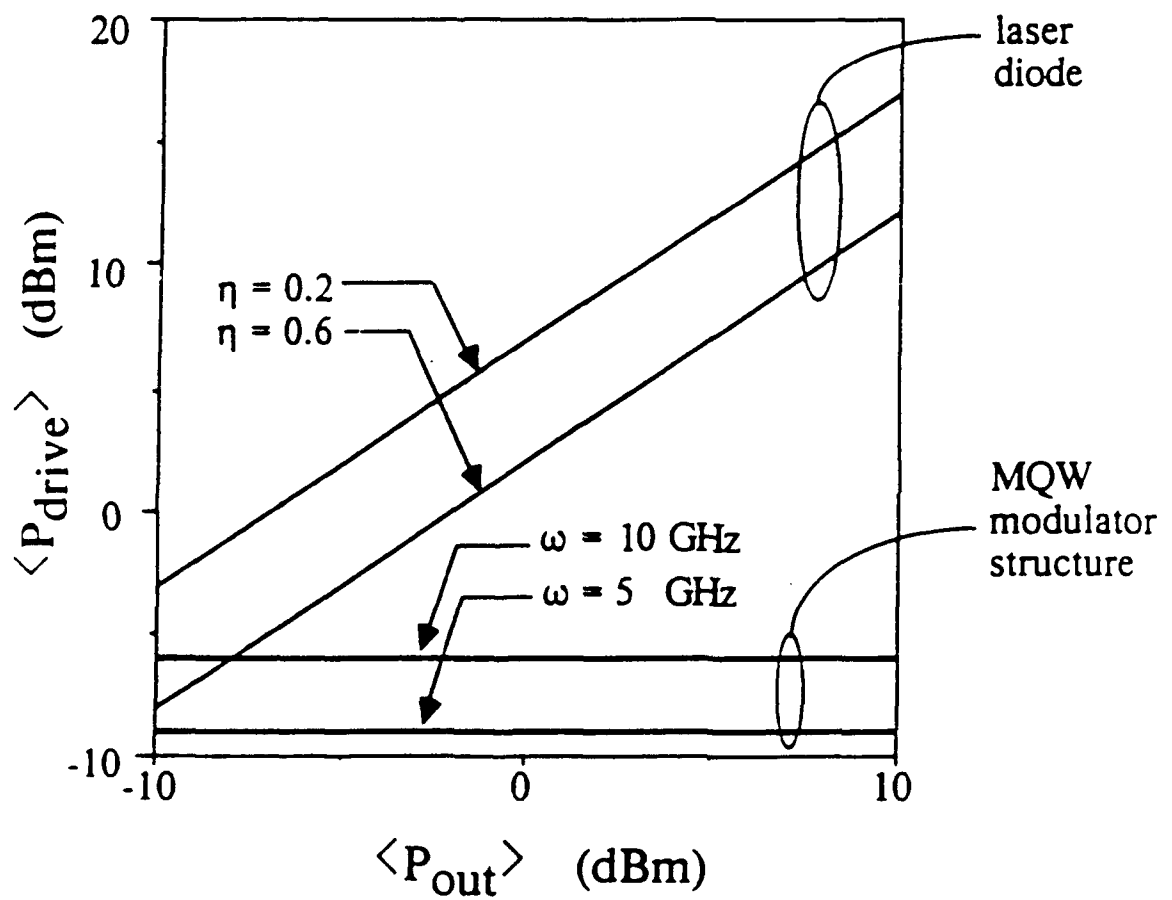
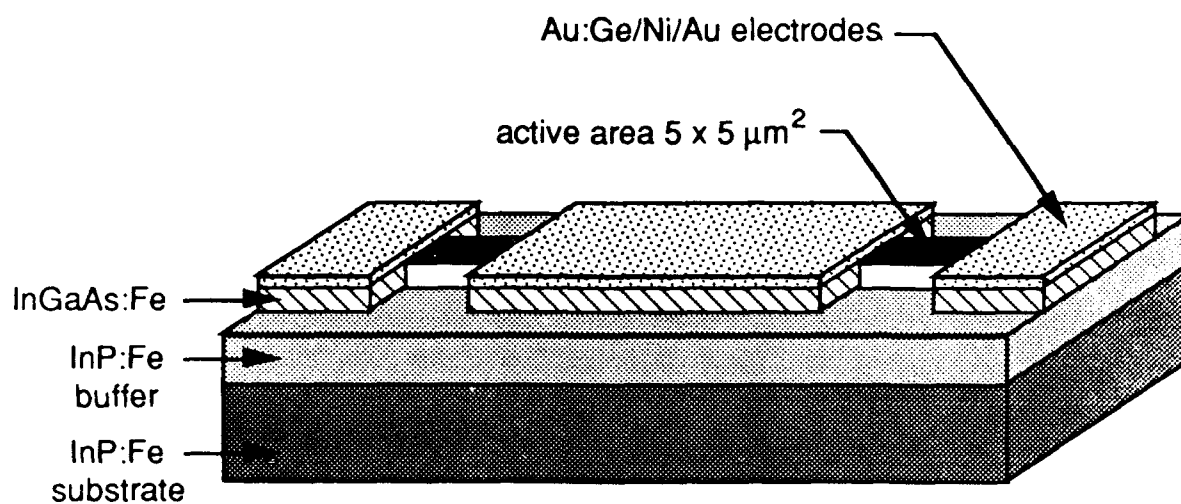**Figure 10** Average electrical drive power of a 20 μm² area device for modulation frequencies of ω = 5 GHz and ω = 10 GHz.

GHz and ω=10 GHz. Note that the electrical drive power is independent of the average optical output power of the modulator

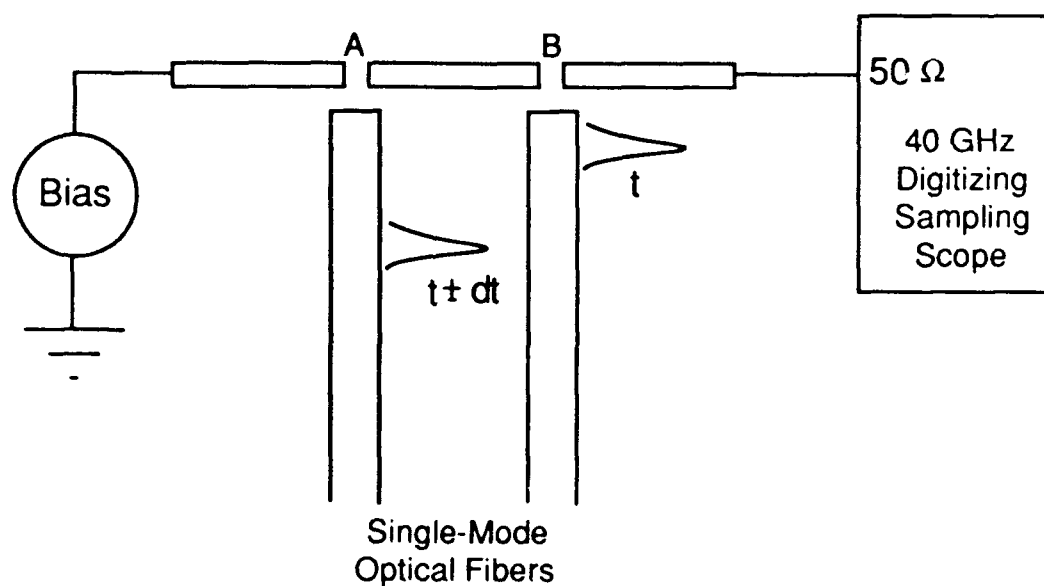$$<P_{out}> = \frac{P_{max} + P_{min}}{2} .$$ (5)

The electrical drive power of a laser diode, on the other hand, is directly proportional to the optical power output, where the constant of proportionality is defined as the external quantum efficiency η. The electrical drive power of a laser diode is also plotted in Fig. 10 as a function of power output, for external quantum efficiencies ranging from η=0.2 to 0.6 (shaded region). It is seen in Fig. 10 that for 0 dBm average optical power output, the MQW modulator requires about 10 dB less electrical drive power than the laser diode, and that this difference increases with optical power output.

3.4 Optical Correlation

In the correlation receiver, a delayed, attenuated version of the framing pulse is correlated with the TDMA frame. This process is equivalent to the logical 'AND' of the framing pulse with the appropriate slot in the TDMA frame. This correlation function has been demonstrated with 2 ps optical pulses using a two-gap photoconductive 'AND' gate shown in Fig. 11a. In brief, the dual-gap photoconductive device consists of a 50 Ω micro-stripline circuit on an insulating substrate connecting two Fe-doped InGaAs photoconductive switches. When light impinges on a photoconductive gap in the electrically-biased stripline, the resistance of the gap changes from high to low, allowing the current to propagate down the stripline. When two optical pulses (each of 2 ps width) simultaneously excite the two photoconductive gaps (points A and B in Fig.11), an electrical pulse appears at the stripline output. On the other hand, if only one gap conducts (the two incident optical pulses do not coincide in time), a spurious signal of low amplitude is observed

3 0

Au:Ge/Ni/Au electrodes

active area 5 x 5 μm^2

InGaAs:Fe

InP:Fe buffer

InP:Fe substrate

(a)

A   B

Bias

50 Ω

40 GHz Digitizing Sampling Scope

t

t + dt

Single-Mode Optical Fibers

(b)

Figure 11   a) Two-gap Fe-doped InGaAs Photoconductive 'AND' gate. b) Optical coupling and electrical biasing arrangement for the correlation measurement.

3 1

at the output. This spurious signal corresponds to dark current through either gap A or B, depending on whether an optical pulse is incident on gap A or B.

A more complete description of the photoconductive AND gate and its operation is now presented with the aid of Figure 11a. The device consists of a 1.4 μm thick layer of Fe-doped $In_{0.53}Ga_{0.47}As$ and a 0.5 μm Fe-doped InP buffer layer grown on a semi-insulating Fe-doped InP substrate by metal organic vapor-phase epitaxy (MOVPE). The electrical contacts consist of Au:Ge/Ni/Au conducting electrodes. Optically sensitive gaps in the electrode were produced by mesa etching and resulted in 5x5 μm square photoconductive gaps. The photoconductive gaps were then ion-damaged with Be at 750 keV with a bombardment dose of 6×10^{10} cm^{-2}. The ion bombardment reduced the free carrier lifetime from greater than 1 ns to less then 150 ps. The electron mobility was found to be 6000 cm^2/V·s by sheet resistance and Hall Effect measurements.[24] The dark resistance of the device was measured to be 19 kΩ.

The operating speed of the gate was determined by using a time-resolved correlation technique. The laser source for this experiment was a Quantronix Model 416 1.319 micron, mode-locked, Nd:YAG laser with 120 ps pulse width and 100 MHz repetition rate. The mode-locked pulses were pulse-compressed using a fiber-grating technique to obtain 2 ps pulses as measured with an optical autocorrelator. The output of the pulse compression system was divided into two equal intensity pulse trains which initially traverse different but equal-length paths. A relative delay was introduced between the two pulse trains by changing the length of one path with a stepping-motor-driven stage. Then, each pulse train was coupled into a short, equal-length single-mode optical fiber. The optical coupling and electrical biasing arrangement of the photoconductive device for the correlation measurement is shown in Figure 11b. Each fiber is butt-coupled to one of the photoconductive gaps. The coupling efficiency between the 10 μm mode field diameter of the optical fiber and the 5x5 μm square gap, assuming a gaussian transverse mode profile, was calculated to be 27%. The optical coupling arrangement delivered 1 pJ optical pulses to both of the photoconductive gaps. The energy incident on each gap was then 270 fJ. A 2.0 V dc bias was applied to the device. The response of the device was monitored by a Tektronix

Model 11801 digitizing, sampling oscilloscope and a Tektronix SD-30 40 GHz sampling head with 50 Ω input impedance.

Figure 12 shows the measured impulse response of each of the photoconductive gaps. The trace denoted by the thin line is the impulse response of gap A. The trace denoted by the thick line is the impulse response of gap B. Each of the traces has the 8 mV dc potential due to the gate dark current removed. As can be seen from this figure, each gap has a similar impulse response. The measured risetime and falltime of the impulse response for each gap was 17 and 21 ps, respectively, and the FWHM was measured to be 24 ps. The fast impulse response of the photoconductive gaps can be attributed to the reduced carrier lifetime in this region resultant from ion-bombardment processing. Indeed, the measured falltime of the response of both gaps suggests that the carrier lifetime is less than 20 ps. However, it should be noted that the measured impulse responses are approaching the measurement limitations of the oscilloscope imposed by the specified 8.8 ps time constant of the sampling head. A very notable feature apparent in the impulse response traces is the existence of slowly decaying, low amplitude tails which persist after the initial fast recovery of the photoconductance. These low amplitude tails have been observed in Si and GaAs photoconductor work performed by others.[25,26] For InGaAs-on-InP systems, the tails have been attributed to surface states or defects resident at the ternary-binary interface which trap and re-emit carriers.[27] From the FWHM of the impulse response data, it would appear as though the device could operate as a logical 'AND' gate at speeds approaching 40 Gbps. However, as will be seen, the slowly decaying tails severely limit the operating speed of the device.

The measured time-resolved correlation data is shown in Figure 13. The vertical axis corresponds to the peak output voltage of gap B at the time t as shown in Figure 11b. The horizontal axis is the time difference dt between the time of arrival of optical pulses at the gaps. Negative horizontal values indicate the optical pulse arriving at gap B is leading the optical pulse arriving at gap A, while positive horizontal values indicate the optical pulse arriving at gap B is lagging the optical pulse arriving at gap A. As in the impulse response measurements, the exciting pulses were 1 pJ, 2 ps optical pulses, and the correlation trace has the 8 mV dc potential from the
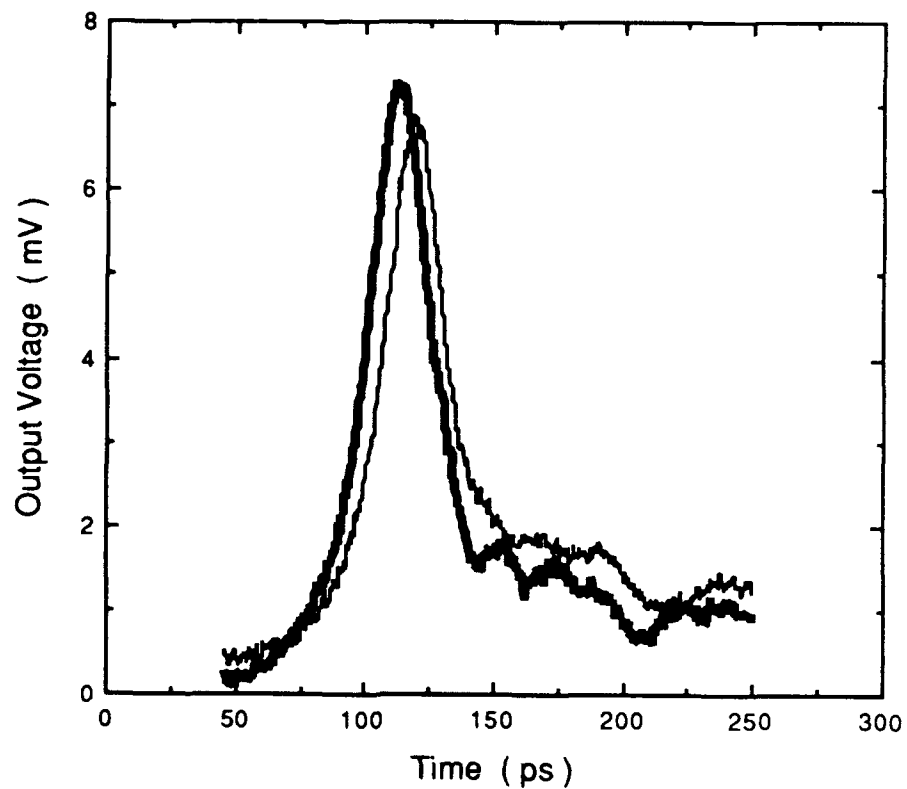
Figure 12 Measured impulse response of each gap of the Fe-doped InGaAs photoconductive 'AND' gate. The thin lines denotes the impulse response of gap A, the thick line denotes the impulse response of gap B.
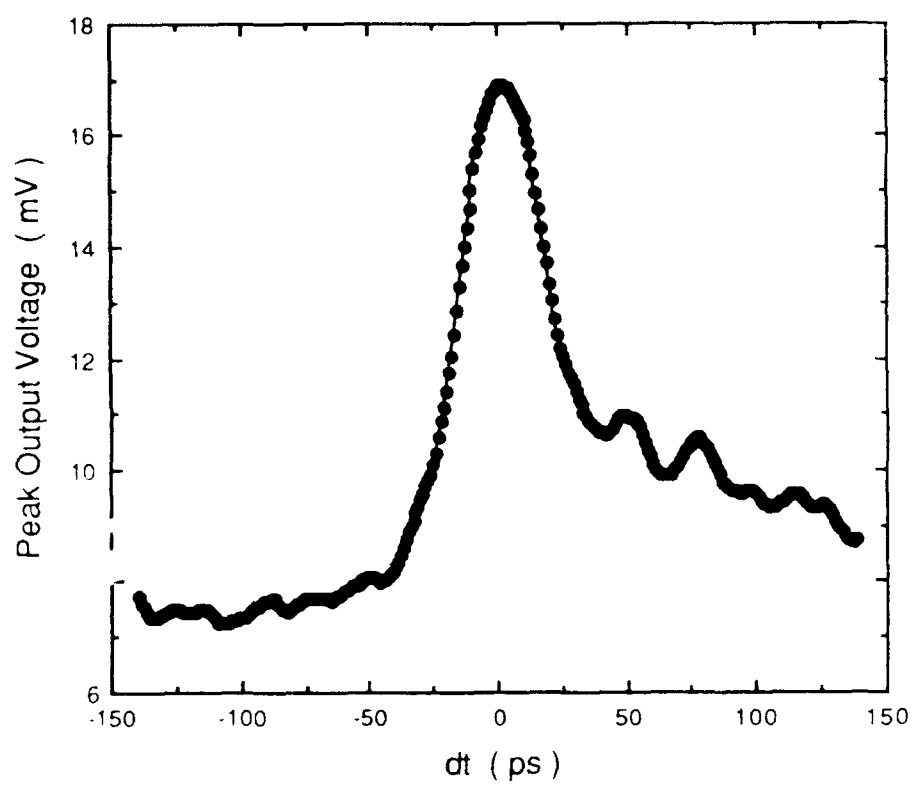
Figure 13 Measured time-resolved correlation data for the photoconductive 'AND' gate.

gate dark current removed. For positive values of dt, the device has a slowly decreasing response. In this region of the curve, the pulse generated at gap B is sampling the tail of the signal generated at gap A. For negative values of dt, the device response is relatively flat. This result is due to the causality of the measurement system, *i.e.* the sampling pulse arrives at gap B before the signal pulse arrives at gap A. In the region around dt = 0, the response resembles the cross-correlation of the individual gap impulse responses.[28] Sampling is not a valid description of the operation of the device in this region since the temporal width of the sampling and signal pulses are similar. If the device is performing a true cross-correlation operation (sampling is a special case of cross-correlation), then the response of the device in the region where dt is negative should be zero because the cross-correlation operation S(T) involves a multiplication,

$$S(T) \propto \int_{-\infty}^{+\infty} f(t)h(t-T) \, dt \qquad (6)$$

where f(t) is the impulse response of gap A and h(t) is the impulse response of gap B. In the case of sampling, h(t) can be approximated by a delta function $\delta(t)$. In this case, the correlation operation becomes,

$$S(T) \propto \int_{-\infty}^{+\infty} f(t)\delta(t-T) \, dt \qquad (7)$$

$$S(T) \propto f(T) . \qquad (8)$$

However, from Figure 13, it is clear that the response of the device is nonzero for negative values of dt. The residual 7.5 mV peak signal is a result of the nonzero dark conductivity of the InGaAs photoconductive gaps.

From a logical 'AND' operation perspective, the nonzero dark conductivity of the gaps reduces the contrast ratio of the device. In this case, contrast ratio is defined as the ratio of the peak output voltage when the arrival of optical pulses on gaps A and B is coincident (*i.e.*, dt = 0) to the peak output voltage when the arrival of optical pulses on gaps A and B differs by a minimum allowable pulse separation t (*i.e.*, dt ≥ t). The minimum allowable pulse separation is dictated by the recovery of the tail associated with the impulse response of the gaps. From Figure 13, it can be seen that the device is fully recovered for values of dt approximately equal to 200 ps. In this case, the contrast ratio is estimated from Figure 13 and found to be 2:1. Thus, the time-resolved measurement has shown the InGaAs 'AND' gate to be capable of operating at 5 GHz (= 1/200 ps) with a contrast ratio of 2:1 at 270 fJ pulse energies incident on the photoconductive gap.

4. Optical TDMA network demonstration at 5 Gb/s

4.1 Experimental setup and results

Using the components previously described, an experimental 5 Gb/s optical TDMA network was constructed. Rather than adding the framing pulse directly to the TDMA frame as described previously and shown in Figure 3, in the experimental configuration of the optical TDMA network we have chosen to deliver the framing pulse directly to the variable-integer-delay line coder, bypassing the star and splitter. This approach was necessary due to power constraints with the photoconductive 'AND' gate. Since the framing pulse no longer frames the multiplexed data, we will refer to it as the clock pulse since this term is more descriptive of its use for optical correlation at the receiver. A schematic diagram of the experimental optical TDMA network developed in this work is illustrated in Figure 14. The primary pulse source for this network is obtained from a Quantronix Model 4217 Nd:YLF, 1.313 μm wavelength, mode-locked laser operating at a 100 MHz repetition rate with 65 ps FWHM pulses. Thus, the system frame period T is 10 ns which is equivalent to a 100 Mb/s baseband data rate. The user time slot τ was set at 200 ps corresponding to a 5 Gb/s multiplexed data rate with N equal to 50 channels. The optical
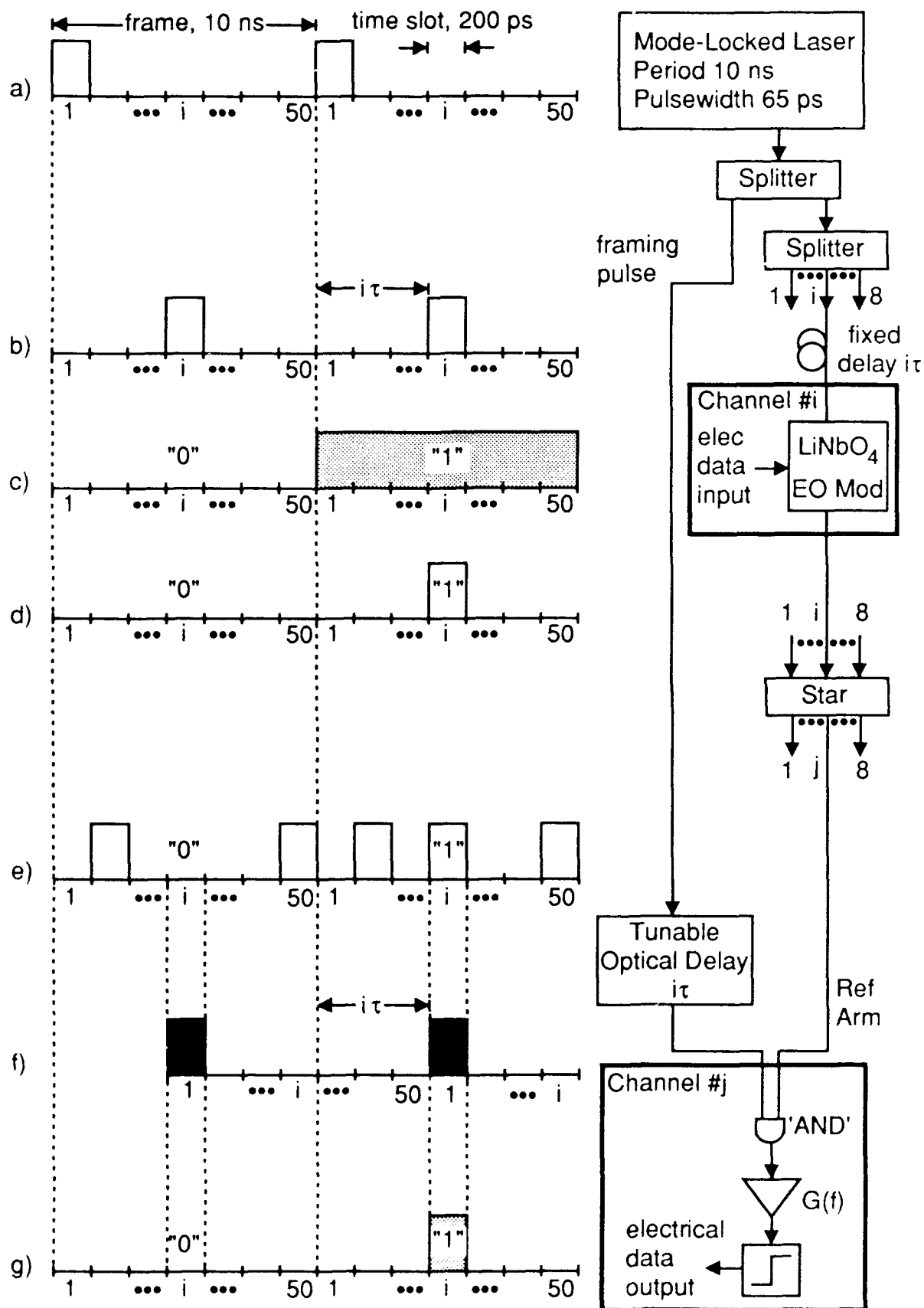
Figure 14 Experimental 5 Gb/s optical TDMA network.

3 8

pulses are passively distributed to the network by a -3 dB 1x2 splitter. This 1x2 splitter performs the task of distributing the clock pulse directly to the variable-integer-delay line coders of the receivers separate from the data pulses.

The data and clock pulses are distributed to the transmitters and receivers, respectively, by two Interfuse 1x8 passive splitters. The typical measured power loss between the input port and any output port for these 1x8 splitters was -8.7 dB. Seven of these output ports were used to transmit data to the network utilizing 14 percent of the network's total capacity. Five of these channels were fixed to transmit all 'ones' data, while the other two channels had full modulation capability. Lithium niobate electro-optic modulators were used to transduce the 100 Mb/s baseband electrical signals onto the optical channels. Polarization dependent Mach-Zehnder modulators with electrical modulation bandwidths of 3 GHz, drive voltages of 8 to 10 V and crosstalk ratios of approximately 31 dB were used in the transmitters. The measured insertion losses of these modulators were -7.3 and -6.7 dB, respectively. These losses are primarily due to waveguide-to-fiber coupling losses. The data channels were then transmitted through fixed optical delays corresponding to integer multiples of the 200 ps user time slot and combined in an Interfuse 8x8 passive star optical coupler. The measured insertion loss between any input port and any output port of the passive star coupler was -9.4±0.3 dB. Now, all of the output ports contain the multiplexed optical data composed of the channels transmitting on the network. One of these output ports is connected to each receiver consisting of a photoconductive 'AND' gate detector, a pre-amplifier and the baseband recovery electronics.

The clock pulse, which bypasses the star, is sent to a variable-integer-delay-line coder capable of coding four user addresses. This variable-integer-delay coder consists of two polarization independent LiNbO$_3$ electro-optic directional couplers, discrete lengths of single mode optical fiber and a 2x1 passive coupler. The total insertion loss of this variable-delay line coder was measured to be -14.7 dB. Each channel receiver has a variable-delay line coder which delivers the clock pulse to an Fe-doped InGaAs photoconductive 'AND' gate for correlation with a time slot

from the multiplexed data stream coming directly from the output of the passive star. The tuning capability of the variable-integer-delay line coder is demonstrated in Figure 15.

The series of traces shown in Figure 15 are the output from the photoconductive 'AND' gate amplified by B&H AC10020H 10 GHz wide band amplifiers and measured with a 20 GHz Hewlett-Packard Model 54120A digitizing oscilloscope. Fig. 15a shows the clock pulse tuned to channel 27 in the 10 ns frame of 50 channels. Channel 27 is not transmitting data, thus correlation with channel 27's address signature results in detection of the clock pulse. The detected pulses shown here are due to the dark current of the photodetector and are an artifact of the non-ideal behavior of the photoconductive 'AND' gate. Fig. 15b shows the clock pulse tuned to channel 1, where the clock pulse is now correlated with the data transmitted in that channel. Fig. 15c shows the clock pulse tuned to channel 2, 200 ps from channel 1 and Fig. 15d shows the clock pulse tuned to channel 26, 5 ns from channel 1.

The electrical output from the photoconductive 'AND' gate is further investigated with the aid of Figure 16. Figure 16a shows the oscilloscope trace of an eye diagram resultant from the correlation of the clock pulse with a psuedo-random data pattern being transmitted in channel 1. The three consecutive pulses correspond to channels #50, 1 and 2 and are displayed on a 100 ps/div timescale. As can be seen from this figure, the contrast ratio or the ratio of the peak signal received when the clock pulse is correlated with a transmitted 'one' to the peak signal received when the clock pulse is correlated with a transmitted 'zero' is approximately 2:1. The energy per optical pulse incident on the photoconductive device was calculated to be approximately 1.4 pJ using the measured average transmitted power per channel and the component insertion loss data. Including the estimated optical fiber-to-ph   conductive gap coupling efficiency of 27%, the energy per optical pulse incident on a photoconductive gap is 378 fJ. An increase in the contrast ratio can be achieved by increasing the energy of the optical pulses incident on the photoconductive gaps. This increase can be realized by reducing the component insertion losses in the network, increasing the optical fiber-to-photoconductive gap coupling efficiency or increasing the energy of the transmitted pulse.
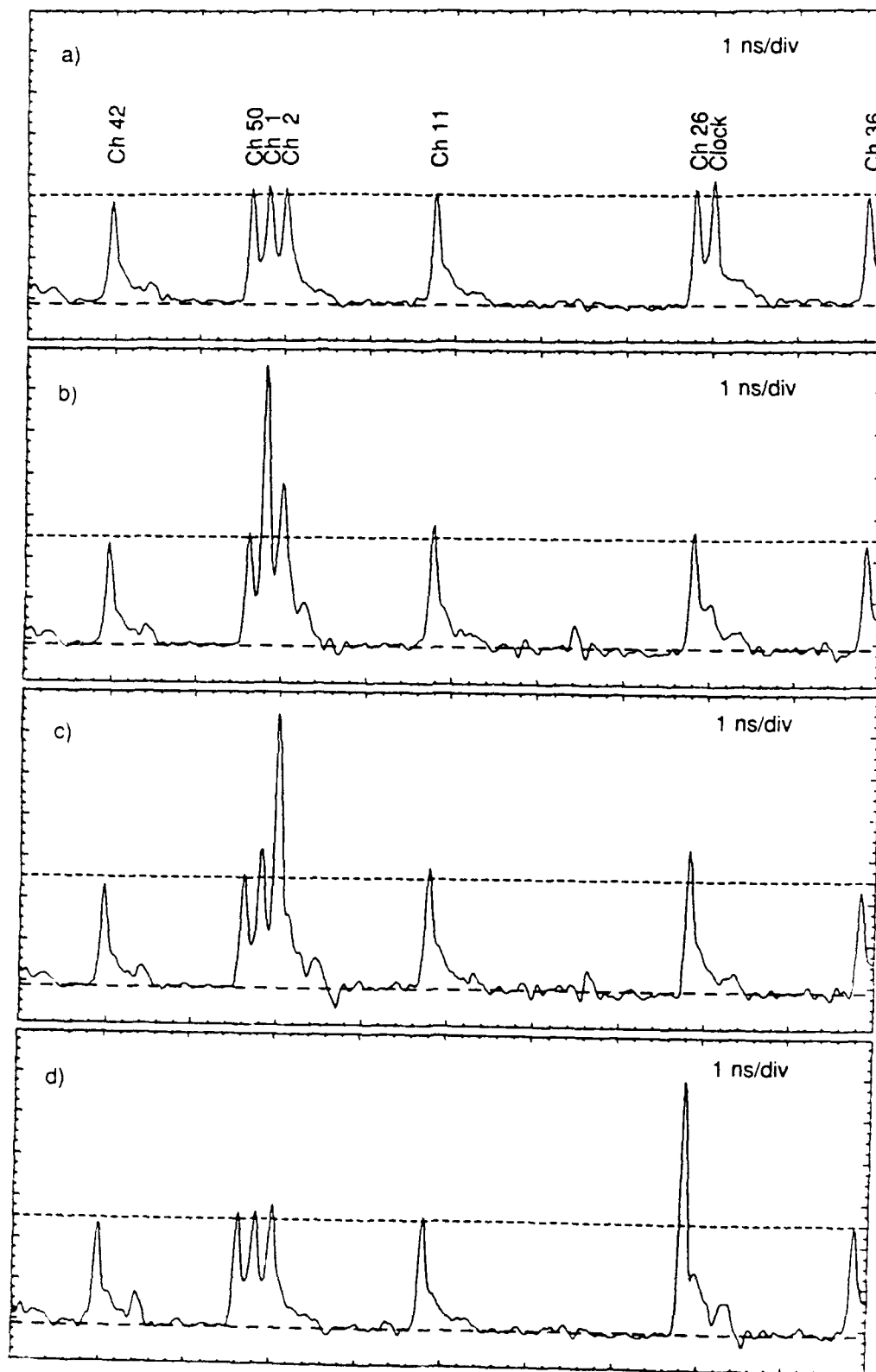
4 0

Figure 15 Demonstration of the multiple-access capability using the optical TDMA coder. Clock pulse tuned to a) channel 27 b) channel 1 c) channel 2 and d) channel 26.
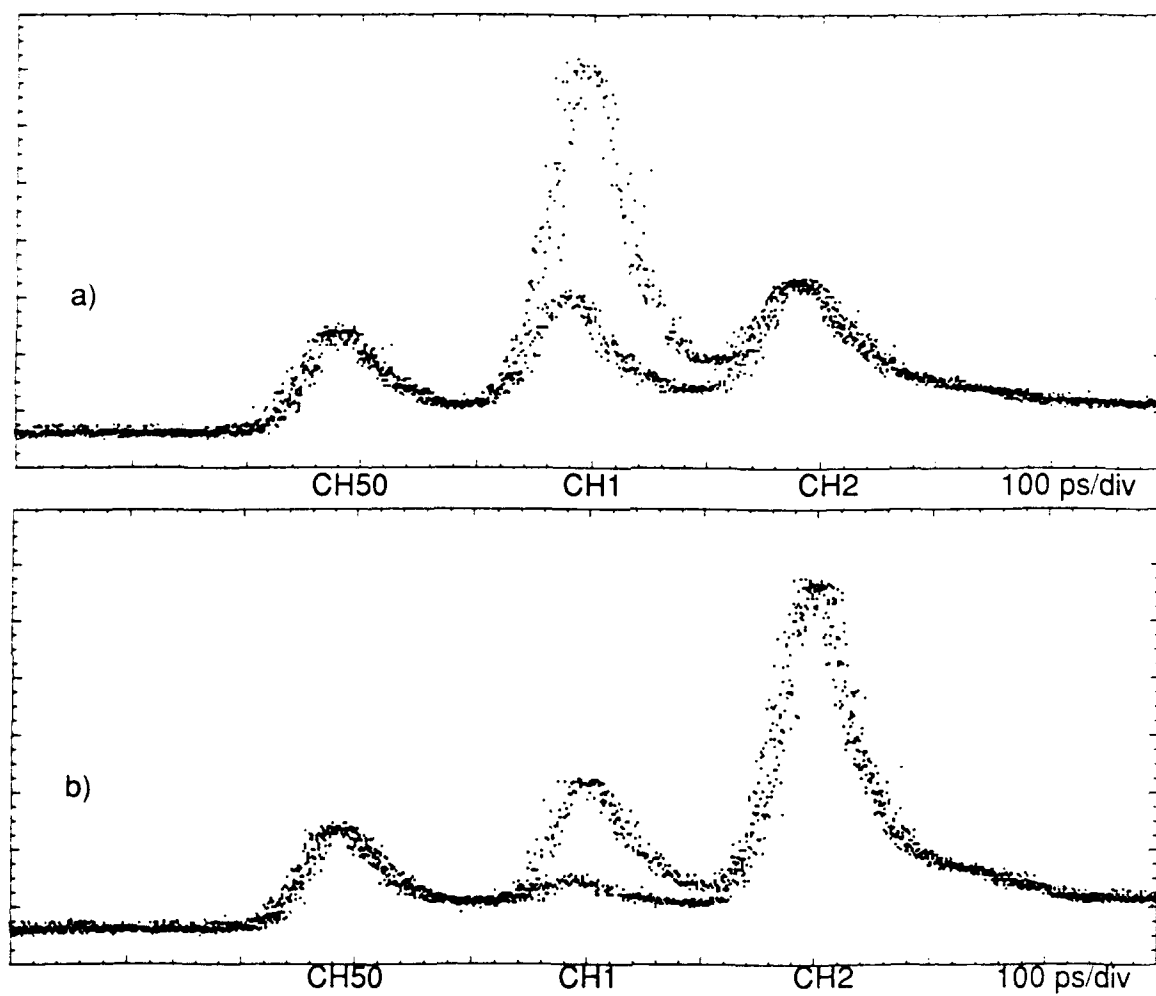
Figure 16   Measured eye diagram of the clock pulse correlated with a) channel 1 transmitting a psuedo-random data pattern, and b) channel 2 transmitting an all 'ones' data pattern.

The low channel crosstalk achievable in the network is indicated by the oscilloscope trace of the clock pulse correlated with an all 'ones' data pattern transmitted in channel 2 while channel 1 transmits a psuedo-random pattern as shown in Figure 16b. Performance of the TDMA network is now limited by the ability to perform the electronic threshold detection of the correlated data from · the photoconductive detector and recover the baseband 100 Mb/s electronic signal. This task was achieved using a high-speed digital integrated circuit as the threshold device and an HP 8082A pulse generator to reconstruct the 100 Mb/s return-to-zero baseband data as shown in Figure 17a. Here, the recovered data for channels 1 (transmitting a 101010 pattern), 2 and 26 (each transmitting an all ones pattern), and 27 (transmitting an all zeros pattern) are obtained by successively tuning the clock pulse to the indicated time slot. Figure 17b is the eye diagram of the channel 1 data recovered from a transmitted pseudo-random bit pattern and illustrates the low noise characteristics of the correlation receiver. The BER for channel 1 was measured to be less than 10^{-9}.

4.2 Noise and BER Analysis

The BER performance of the photoconductive AND gate is dependent not only on the contrast ratio of the device, but also the noise characteristics of the photoconductor itself and the surrounding electronic circuitry. The noise current generator equivalent circuit model used for the AND gate is shown in Figure 18. To simplify the analysis, only one of the 10 GHz pre-amplifiers necessary for the receiver circuitry has been included in the noise and BER analysis. The noise generated in the photoconductive gate consists predominantly of generation-recombination and thermal noise, modeled as noise current sources i_{Ngr} and i_{Nt}, respectively. The mean-squared generation-recombination noise term $<i_{Ngr}^2>$ is similar in form to shot noise. However, for photoconductors the photoconductive gain τ_o/τ_d must be included in the noise estimation, where τ_o is the hole lifetime and τ_d is the electron transit time across the photoconductive gap. The addition of the photoconductive gain in the generation-recombination noise equation is the origin of a term
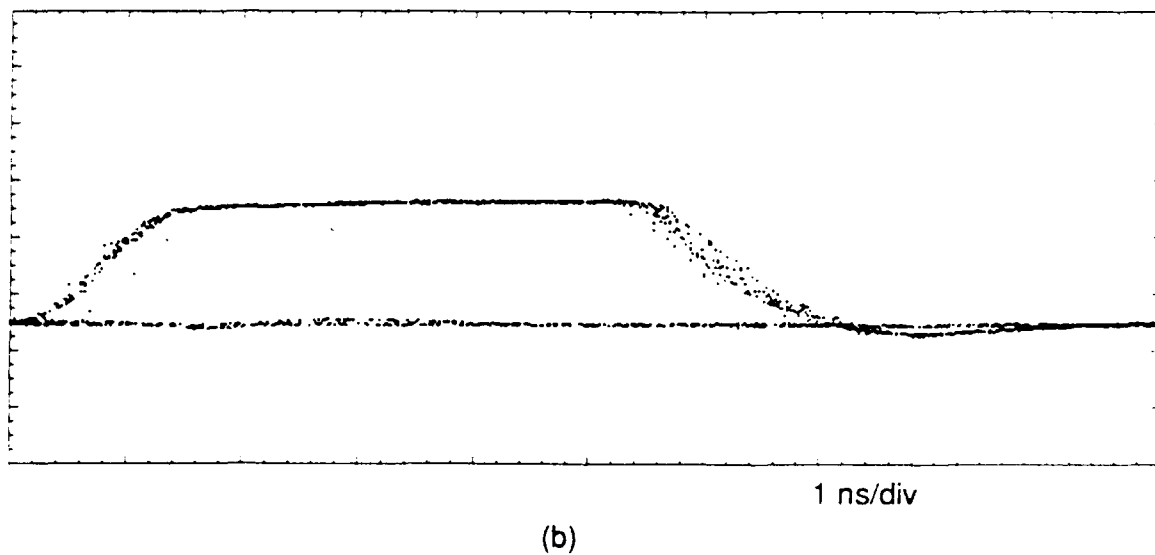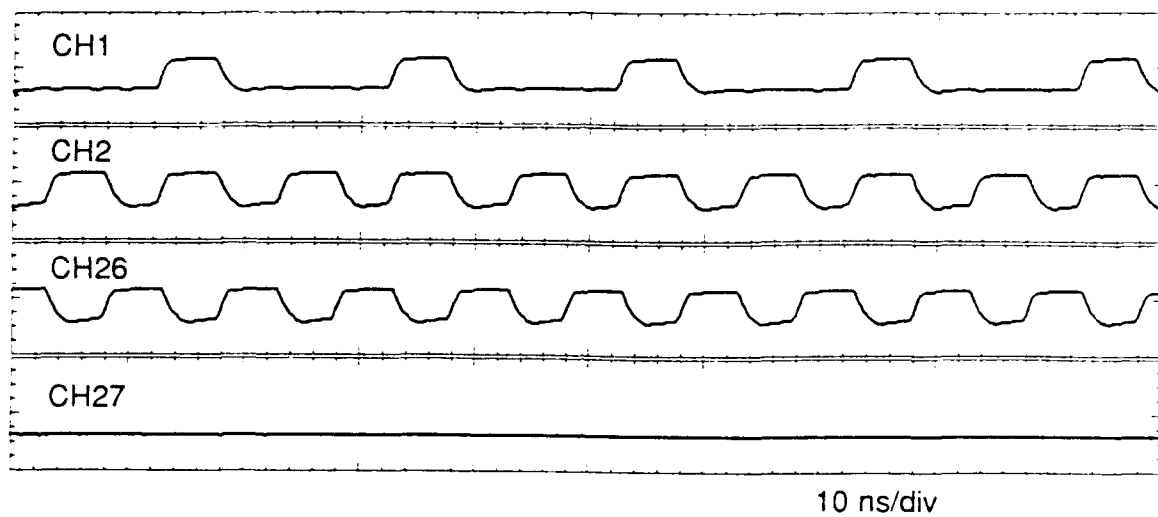
43

Figure 17 a) Recovered 100 Mb/s RZ baseband data in channel 1 transmitting a 1010 pattern, channels 2 and 26 transmitting all ones, and channel 27 transmitting all zeros. b) Eye diagram of recovered baseband pseudo-random data being transmitted in channel 1.
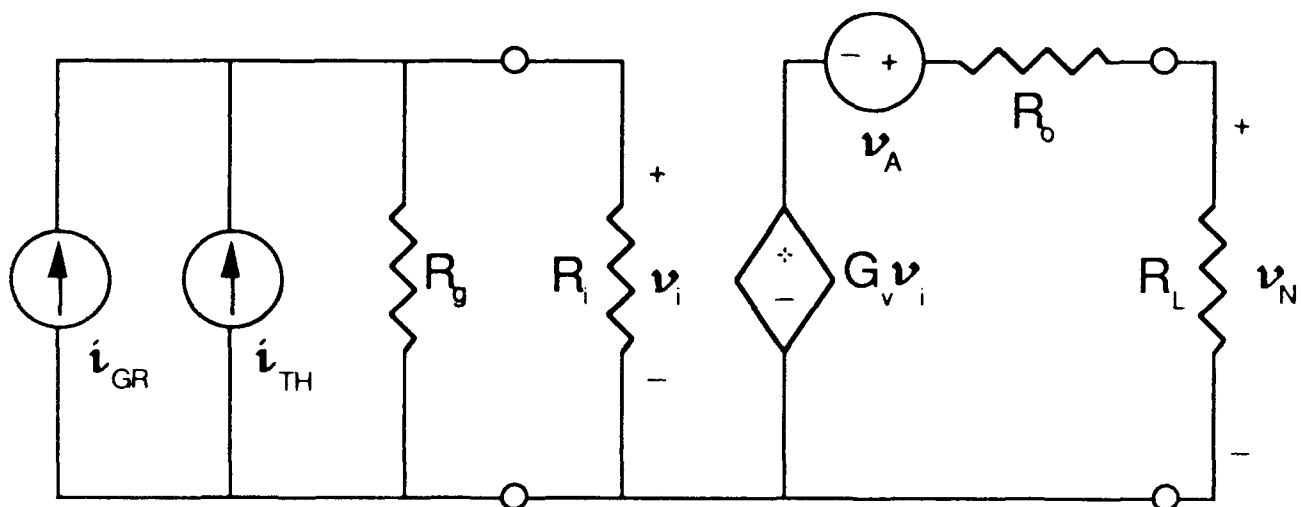
44

Figure 18 Noise current generator equivalent circuit model used for the noise and bit-error-rate analysis of the photoconductive 'AND' gate.

that decreases as 1/n, where n is frequency.[28] The amplifier contributes its own noise to the system as shown by the noise voltage source at the output of the amplifier in Figure 18. The amplifier mean-squared noise voltage can be written as,

$$<v_{Na}^2> = 4 \, k \, (F - 1) \, 290 \, \Delta v \, R_i .$$

(9)

The mean-squared noise currents for the gate are estimated from,

$$<i_{Ngr}^2> = 4e\Delta v \left(\frac{\tau_o}{\tau_d}\right)\left[\frac{<i_s>}{1 + 4\pi^2\tau_o^2v^2} + i_d\right]$$

(10)

$$<i_{Nt}^2> = \frac{4kT\Delta v}{R_g} ,$$

(11)

The terms used in Equations (9), (10), and (11) are defined as,

$<i_s>$ = mean signal current in one bit period (312.8 µA),

T = room temperature (290 K)

i_d = gate dark current (160 µA),

Δv = circuit bandwidth (10 GHz),

v = reference frequency (0 Hz),

e = electron charge (1.602×10^{-19} C),

τ_o = hole lifetime (< 20 ps),

τ_d = electron transit time (42 ps),

k = boltzmann's constant (1.381×10^{-23} J/K),

F = amplifier noise figure (5),

R_g = gate dark resistance (19kΩ),

R_i = amplifier input impedance (50 Ω).

The mean-squared noise voltage at the output of the amplifier is given by

$$<v_N{}^2> = \left(\frac{1}{2}\right)^2 \left[<v_{Na}{}^2> + \left[\frac{G_v R_g R_i}{R_g + R_i}\right]^2 (<i_{Nt}{}^2> + <i_{Ngr}{}^2>) \right] .$$ (12)

Where G_v is the voltage gain of the amplifier, measured to be approximately 5. The calculated noise power for the amplifier, generation-recombination, and thermal noise sources at the output of the amplifier are -67.9 dBm, -67.5 dBm, and -85.8 dBm respectively. From these values, it is clear that the AND gate circuit is dominated by amplifier and generation-recombination noise. For the case of coincident clock and signal pulses, substitution of the numeric values shown above into Equation (12) result in a calculated noise power of -64.7 dBm over the 10 GHz bandwidth of the AND gate circuit. The calculated signal power for this case, using experimental data similar to the data shown in figure 16 and including a voltage gain of 5, is -8 dBm. The resultant theoretical signal-to-noise ratio (SNR) is 56.7 dB. The low-noise characteristics of the gate become even more evident when the calculated noise power is normalized to a one hertz frequency band. This results in a noise power spectral density of -104.7 dBm/Hz.

The low-noise characteristics of the gate were verified using a Hewlett-Packard 70000 Series, 22 GHz spectrum analyzer, with a noise power spectral density of -147 dBm/Hz (measured with a 50 Ω load). The measured frequency spectrum of the gate output over a 12 GHz band is shown in Figure 19, and the noise power of the output spectrum is seen to be approximately -65 dBm. This measured value is in good agreement with the calculated noise power. Clearly, the high SNR of the photoconductive AND gate should lead to satisfactory BER performance despite the low contrast ratio of the device.

Indeed, the BER of the photoconductive AND gate operating at 5 Gbps can be estimated from the following expression, assuming gaussian statistics and equiprobable 1 and 0 events,
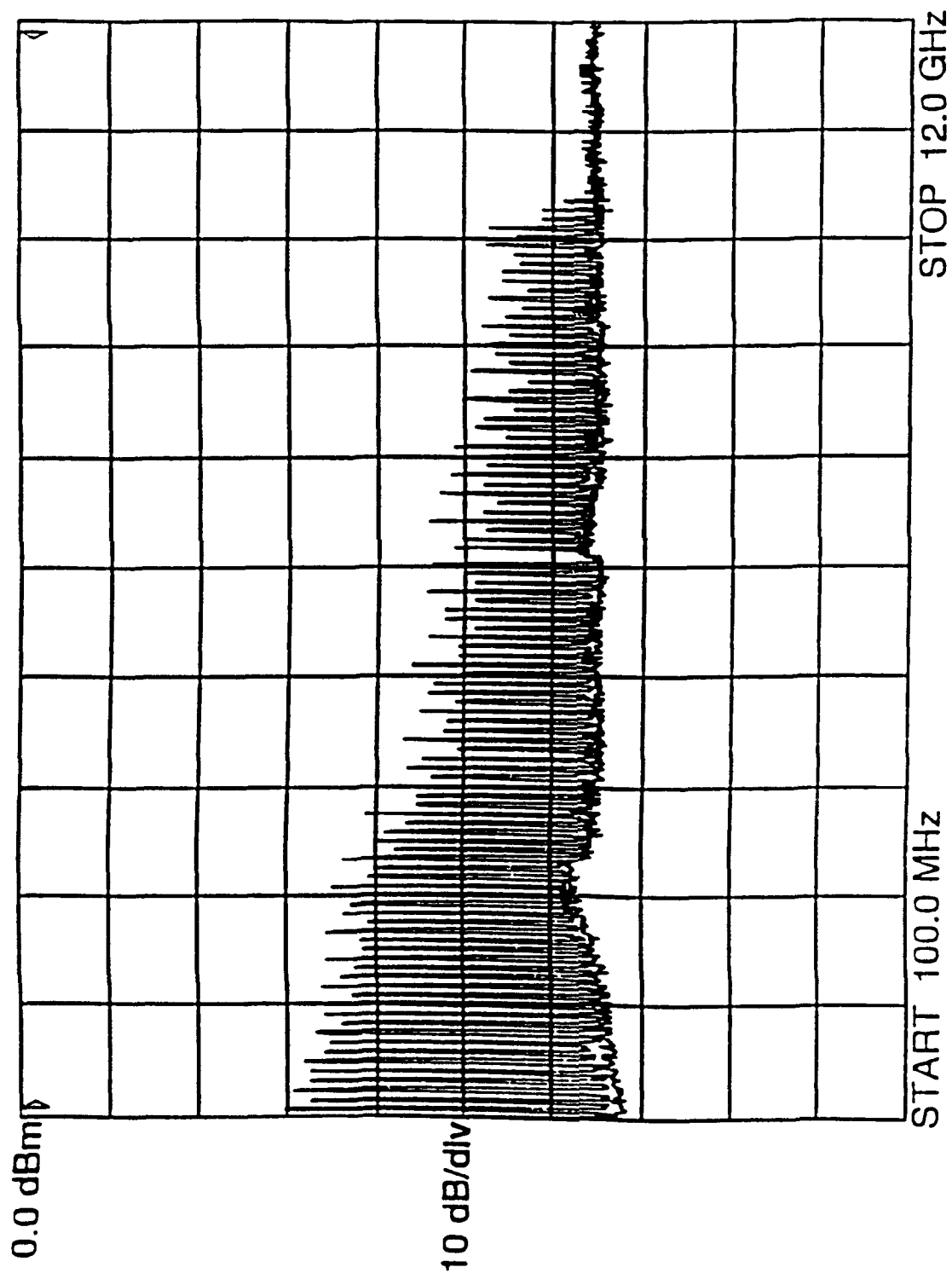
47

Figure 19 Measured frequency spectrum of the photoconductive 'AND' gate over a 12 GHz band.

$$P_e = \frac{1}{2\sqrt{2\pi}\,\sigma_1} \int_{-\infty}^{v_T} \exp\left[- \frac{(v - <v_1>)^2}{2\,\sigma_1^2} \right] dv \;\; +$$

$$\frac{1}{2\sqrt{2\pi}\,\sigma_0} \int_{v_T}^{+\infty} \exp\left[- \frac{(v - <v_0>)^2}{2\,\sigma_0^2} \right] dv \;. \quad (13)$$

After some algebra, Equation (13) can be reduced to

$$P_e = \frac{1}{4} \left[erfc\left(\frac{<v_1> - v_T}{\sqrt{2}\,\sigma_1} \right) + erfc\left(\frac{v_T - <v_0>}{\sqrt{2}\,\sigma_0} \right) \right]. \quad (14)$$

The terms in Equation (14) are defined as,

v_T = threshold voltage,

$<v_1>$ = mean signal voltage in one bit period when a 1 is received,

$<v_0>$ = mean signal voltage in one bit period when a 0 is received,

$\sigma_1 = \sqrt{<v_N^2>}$, rms noise voltage when a 1 is received,

$\sigma_0 = \sqrt{<v_N^2>}$, rms noise voltage when a 0 is received.

The rms noise voltages, σ_1 and σ_0, have values of 130.8 and 118.9 μV respectively. The mean signal voltages $<v_1>$ and $<v_0>$ are 78.2 and 39.1 mV, respectively, as evaluated from recorded data. The threshold voltage for the BER calculation was set at the mean of $<v_1>$ and $<v_0>$, *i.e.* v_T = 58.66 mV. The small rms noise voltages with respect to the mean signal voltages result in a calculated BER of less than 10^{-15}.

4.3 Power budget analysis

The maximum size of the TDMA network is limited by either the duty cycle of the mode-locked laser or the optical power budget. A mode-locked pulse-compressed laser with less than 2 ps pulses would permit N=5,000 time slots in a T=10 ns TDMA frame. However, the question then arises as to whether the transmitter can deliver sufficient energy to the receiver to recover the data with less than a 10^{-9} BER, taking into account the splitting and excess losses in the system. The experimental network demonstrated in this work is power budget limited, due to the high insertion losses of the electro-optic modulators and switches.

Theoretically, in the self-clocked network architecture, if the energy per pulse from the optical source is E_L, and the total optical loss in the system is L (dB), then the energy E_d reaching the detector is

$$E_d = E_L 10^{-\left(\frac{L}{10}\right)} \quad [J],\tag{15}$$

where

$$L = L_{mod} + L_{cod} + 3 - 10\log(\beta) + 10\log(N) \quad [dB].\tag{16}$$

Here L corresponds to the case where an array of N synchronous mode-locked lasers are used and β is the modulation depth. The last term represents the splitting loss in the star coupler. If instead a single mode-locked laser is used, it would be followed by a 1xN splitter (as shown in Fig.2) and N in the last term would be replaced by N^2. The loss of 3 dB in this expression corresponds to the splitting loss at the input to the receiver. The excess loss in the coder L_{cod} depends on the

50

number of stages, and can be quite large. As an example, we will assume that the entire coder is integrated on a single substrate, so that the insertion loss is primarily due to the fiber-to-waveguide and waveguide-to-fiber coupling, which we assume to be a total of 6 dB, and the loss per stage is assumed to be 1 dB. Thus, L_{cod} is given as,

$$L_{cod} = 6 + 1 * \lceil \log_2(N) \rceil \quad [dB]. \tag{17}$$

The excess loss in the modulator L_{mod} is taken to be 3 dB, and the modulation depth is assumed to be unity. Finally the energy per pulse produced by each laser is taken to be E_L=20 nJ.

With these assumptions, the energy reaching the detector is plotted as a function of N in Figure 20 for the case of an array of N synchronous mode-locked lasers (dashed line) and the case of a single mode-locked laser (solid line). In order for the receiver to recover the data with an acceptable bit error rate (*i.e.* < 10^{-9}), the sensitivity of the detector must be less than the received energy. The sensitivities of several detectors at 1.3 µm are indicated in Fig.7, including the photo-conductive AND gate (250 fJ), a pn diode (8 fJ), a pin diode (0.32 fJ), an avalanche photodiode (15.8 aJ) and the quantum limit (3.2 aJ). With the photoconductive 'AND' gate, which has rather poor sensitivity, the number of nodes that can be accommodated in the network is between about N=15 and N=1000, depending on whether a single laser or array of lasers is used. For more sensitive detectors, the allowed number of nodes on the network increases rapidly.

5. Summary

Optical micro-area and local-area networks can provide flexible communications among VLSI processors and eliminate electrical I/O bottlenecks. Shared-medium multiple access protocols avoid the access delays associated with statistical multiple access protocols (which are unacceptable in multiprocessor applications) and increase the throughput of high data-rate
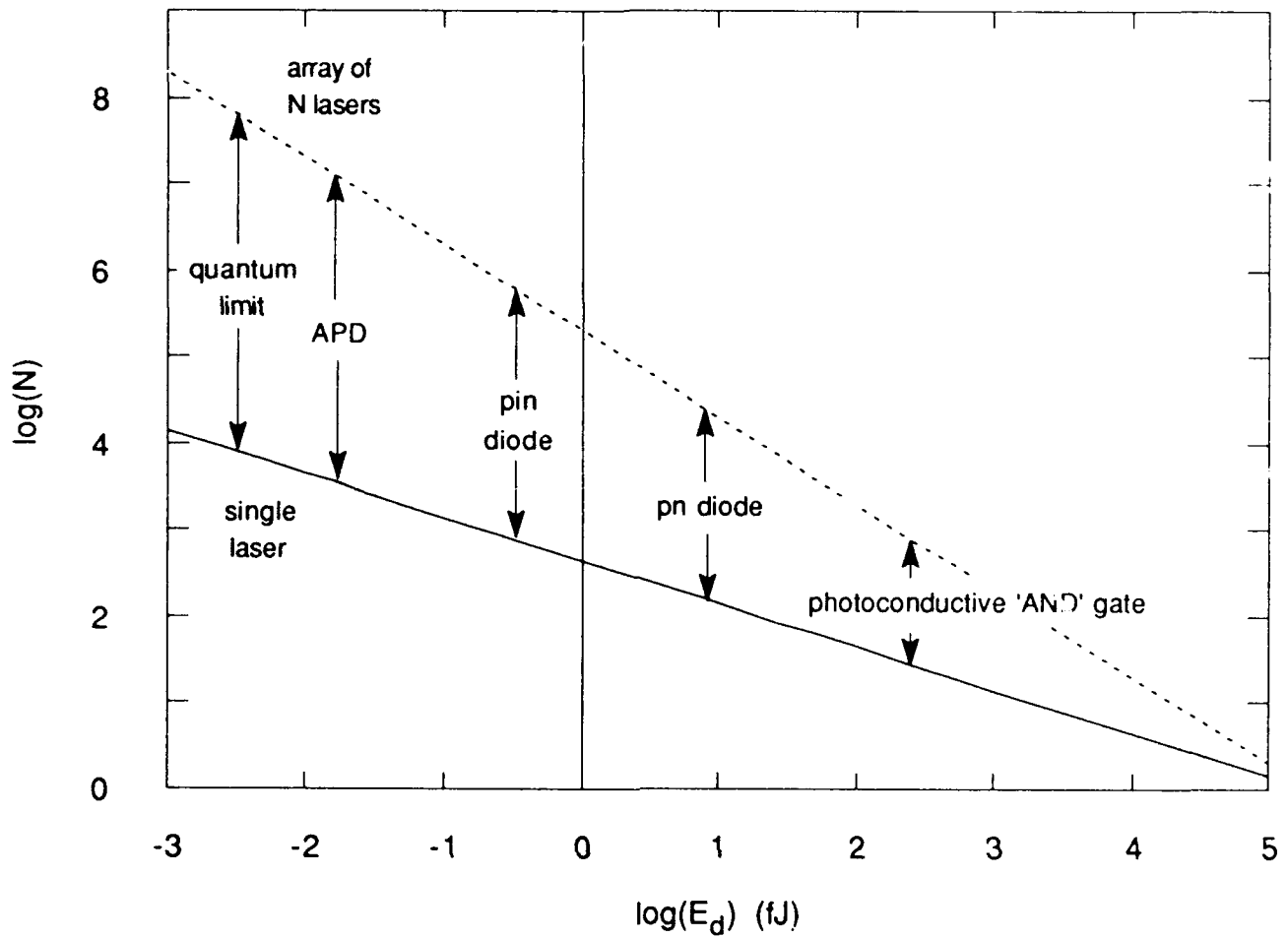
51

Figure 20   Number of users N plotted as a function of the bit-energy reaching the detector. Several detector sensitivities are shown on the plot.

networks, at the expense of wasting the fiber's bandwidth. Time-division multiple access (TDMA) may be more practical to implement in an optical network than other shared-medium multiple access protocols such as frequency-division or code-division.

Since the total throughput of TDMA is given by $1/\tau$, the throughput can be increased by making τ small. Accomplishing this goal requires avoiding the use of low-bandwidth electronics in the portion of the network that directly processes these short pulses. Instead, optical processing can be used in those portions of the network. The architecture of a TDMA network which uses optical multiple access processing and is self-clocking was described in detail. Experiment demonstrations of key subsystems for optically generating, modulating, synchronizing, delaying and correlating short optical pulses were presented.

The feasibility of a variable-integer-delay line which provides rapid tuning, wide tuning range and high precision was investigated and demonstrated for $N=64$ 100 Mbit/sec channels ($T=10$ nsec and $\tau=156.25$ psec). A delay-line capable of addressing $N=1000$ 1Gbit/s channels with subnanosecond reconfiguration time appears to be feasible.

The main reason a mode-locked laser with an external modulator is used in the TDMA μAN is that arbitrarily short pulses ($\tau<1$ psec) can be modulated with a modulator that need only operate at the bit rate $1/T$, which in turn provides extremely high total throughput ($1/\tau >1$ THz). The use of an off-chip optical source and an on-chip modulator also has circuit-integration advantages over a laser diode, including lower electrical drive power, electrical drive power that is independent of output optical power, greater ease of hybrid integration on silicon substrates, and less required real-estate on the chip. Experimental measurements of the modulation depth, excess transmission loss and required electrical drive power of an MQW modulator were presented and related to system performance.

The optical correlation receiver was demonstrated using 2 psec optical pulses and a two-gap photoconductive 'AND' gate. The sensitivity, rise-time and fall-time of the device were measured. The demonstration of a 5 Gb/sec optical TDMA network was presented, and its performance was analyzed.

5 3

The maximum size of the TDMA network is limited by either the duty cycle of the mode-locked laser or the optical power budget. The mode-locked pulse-compressed laser used would permit N=5,000 τ=2 psec time slots in a T=10 ns TDMA frame (*i.e.*, 5,000 100 Mbit/s users). Given the 20 nJ pulse energy produced by the laser, the 250 fJ sensitivity of the photoconductive AND gate, the splitting loss in the star coupler, and the excess loss (3 dB) and modulation depth (assumed to be unity) of the modulator , the excess loss of the variable optical delay, the power budget of the TDMA network was calculated. From power budget considerations, on the order of N=1000 nodes in the TDMA network is possible.

Using the values assumed in the last section, we have presented an optimistic picture of the performance of an optical TDMA network. In reality, much advancement in selected areas of photonics and electronics needs to be achieved before large optical networks of this or any type can be implemented in the field. For example, as evidenced from the experimental network previously presented, very high insertion losses were encountered in incorporating the lithium niobate modulators into the system. Indeed, fiber-to-waveguide and waveguide-to-fiber coupling efficiency improvements are extremely important in attaining the low insertion loss requirements of L_{mod} and L_{cod} in Equ. 16.

Also of great importance are improvements in the high-speed detection and thresholding of the optoelectronic receiver. As presented, the current photoconductive 'AND' gate has operating speeds of at least 5 Gbps. However, the non-ideal behavior of operation resultant from the gap leakage currents places stringent requirements on the electronic thresholding device. This thresholding device must have GHz bandwidth in order to follow the fast rising edge of the incoming signal (see Fig. 16), and have the sensitivity to trigger a pulse when thresholding in a selected time slot, while not integrating over successive time slots. This behavior is not readily available with current commercial electronics, thus improvements in the photonic device's correlation operation (*i.e.* a more ideal 'AND' operation) is needed.

One method under investigation is to use an all optical logic device such as a multiple quantum well (MQW) etalon. Such a device would be designed to perform the thresholding

function based on input optical intensity. As illustrated in Fig. 21, incoming multiplexed data pulses have optical intensities below the threshold level and do not affect the resonant characteristics of the etalon. These optical pulses are blocked by the device. However, when the framing and data pulses are coincident, a larger optical intensity is incident on the device that changes the resonant characteristics of the etalon. The device becomes more transparent and allows the coincident optical data pulse to pass through, forming the demultiplexed data stream. The demultiplexed data would subsequently be photodetected and converted to the baseband electrical signal.

Now, the demultiplexing burden is on the speed of the optical etalon device. These devices also need high bandwidths in order to follow the rising edge of the incoming signals and recover before the next time slot arrives. Etalon devices typically have turn-on times of less than 1 ps, however, the recovery time of these devices can be on the order of nanoseconds. Recently, we measured an MQW etalon with a recovery time of approximately 175 ps.[29] This recovery time is on the order of what is necessary for an all optical logical 'AND' gate to work in Gbps optical TDMA networks.
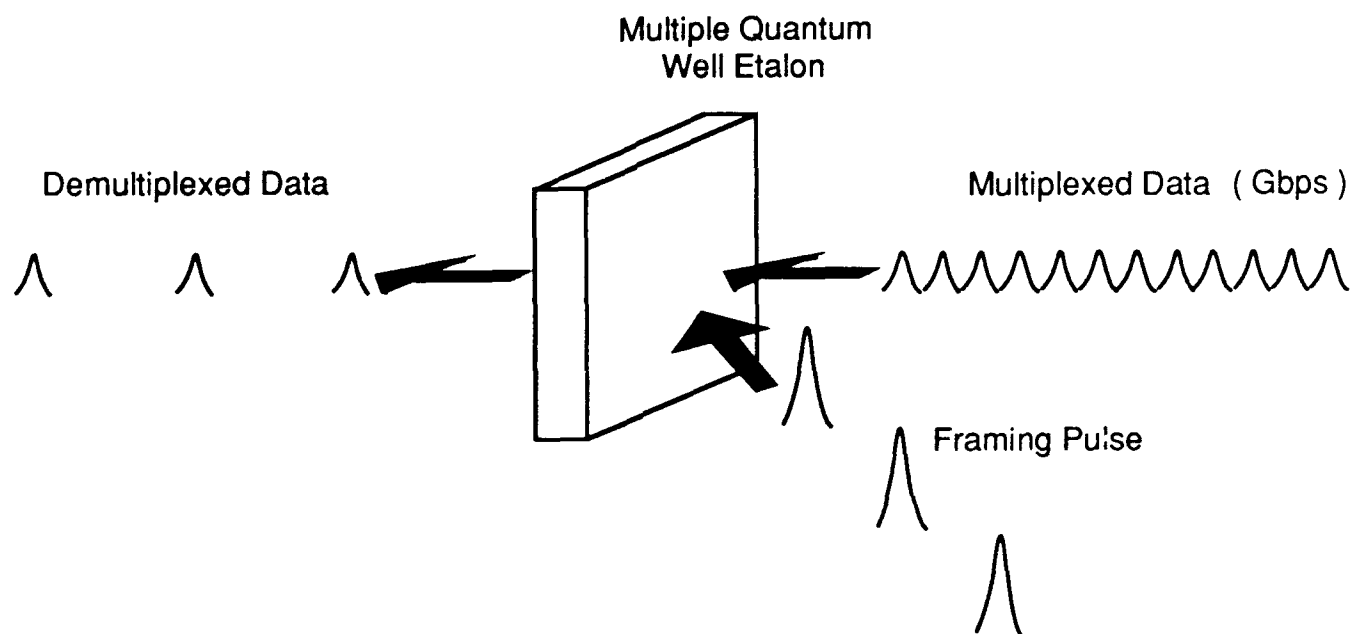
6. Acknowledgements

Figure 21 Illustration of the use of a multiple quantum well nonlinear etalon as a demultiplexing element in an optical TDMA network.

7. References

1.   R.W. Keyes, "Physical limits on digital electronics," Proceedings of the IEEE, Vol. 63, No. 5, pp. 740-767, 1975.

2.   J.W. Goodman, F.J. Leonberger, S.Y. Kung, and R.A. Athale, "Optical interconnections for VLSI systems," Proceedings of the IEEE, Vol. 72, No. 7, pp. 850-865, 1984.

3.   Prucnal, P.R. (1986). " VLSI fiber optic LAN," *Proc. International Optical Computing Conf.*, (North-Holland, NY) J. Raviv, Ed., **700**, 230-238.

4.   Prucnal, P.R. (1986). "VLSI optical interconnection networks," *SPIE Proc. Integration and Packaging of Optoelectronic Devices*, (SPIE, Bellingham, WA) **703**, 106-115.

5.   Prucnal, P.R. (1986). "Optical interconnections for VLSI local area networks," *IEEE Electrotechnology Rev., 97-98.*

6.   Elby, S.E. and Prucnal P.R. (1988). "Fiber-optic interconnect devices for VLSI micro-area networks," *Proc. Soc. Photoopt. Inst. Eng.* (SPIE, Bellingham, WA) **994**, pp.77-91.

7.   Prucnal, P.R. and Perrier, P.A. (1989). "Optical interconnect switch," *Proc. Soc. Photoopt. Inst. Eng.* (SPIE, Bellingham, WA), in press.

8.   Prucnal, P.R. (1989). "An optical interconnect switch,"*Proc. Materials Res.. Soc.*, (MRS, Pittsburgh, PA) 354.

9.   Stallings, W., Local Networks. An Introduction (Macmillan, NY, 1984).

10.   Linke, R.A., "Frequency division multiplexed optical networks," IEEE Network Magazine, Vol. 3, No. 2., pp. 13-20, 1989.

11.   Kaminow, I.P., "Non-coherent photonic frequency-multiplexed access networks," IEEE Network Magazine, Vol. 3, No. 2., pp. 4-12, 1989.

12.   Perrier, P.A. and Prucnal, P.R. (1988). "Wavelength-division integration of services in fiber-optic networks," *International J. of Analog and Digital Cabled Systems*, 1 #3, 149-157.

13.   Prucnal, P.R., Santoro, M.A. and Fan, T.R. (1986). "Spread spectrum fiber optic local area network using optical processing," *IEEE J. Lightwave Tech.*, LT4 #5, 547-554.

14.   Prucnal, P.R., Santoro, M.A., and Sehgal, S.K. (1986). "Ultrafast all-optical synchronous multiple access fiber networks," *IEEE J. Select. Areas Communic.*, SAC-4 #9, 1484-1493.

15.   Santoro, M.A. and Prucnal, P.R. (1987). "Asynchronous fiber optic LAN using CDMA and optical correlation," *Proc. IEEE*, 75 #9, 1336-1338.

16.   Kwong, W.C. Perrier, P.A. and Prucnal, P.R., "Performance comparison of code-division multiple access and synchronous spread spectrum multiple access," *IEEE Trans. Comm.*, in press.

17.   Prucnal, P.R., Santoro, M.A., Sehgal, S.K., and Kaminow, I.P. (1986). "TDMA fiber optic network with optical processing," *Elec. Lett.*, **22** #23, 1218-1219.

18.   Prucnal, P.R., Blumenthal, D.J. and Santoro, M.A. (1987). "A 12.5 Gbps fiber-optic network using all-optical processing," *Elec. Lett.*, **23** #12, 629-630.

19.   Thompson, R.A. ``Optimizing photonic variable-integer-delay circuits," Topical Meeting on Photonic Switching (Inciude Village, NV, 18-20 March 1987), Technical Digest, Vol. 13, paper FD4, 241-143.

20.   Prucnal, P.R., Krol, M F., and Stacy, J.L., "Demonstration of a rapidly tunable optical time-division multiple-access coder," IEEE Photonics Tech. Lett., **3** (2), 170 (1991).

21.   Goossenn, K.W. et al.(1989) "GaAs-AlGaAs Multiquantum well refection modulators grown on GaAs and silicon substrates," *IEEE Photonics Tech. Lett.*, 1 #10, 304-306.

22.   Goodhue, W.D. et al., (1986) "Quant":m well charge-coupled device-addressed MQW spatial light modulators," *J. Vac. Sci Tech.* B4, 769-772.

23.   H.S. Cho, and P.R. Prucnal, "Effect of parameter variations on the performance of GaAs/AlGaAs multiple quantum well electroabsorption modulators," IEEE J. Quantum Elect., **25**, (1989).

24.   E. Desurvire, B. Tell, I. P. Kaminow, K.F. Brown-Goebeler, C.A. Burrus, B.I. Miller, and U. Koren, "1 GHz GaInAs:Fe Photoconductive Optical AND Gate with ~100 fJ Switching Energy for Time-Division Access Networks," Electronic Letters, **25** (2), 105 (1989).

25.   C.H. Lee, <u>Picosecond Optical Devices</u>, (Academic Press Inc., Orlando, FL, 1984, pp. 73-117).

26.   M. B. Johnson, T. C. McGill, and N. G. Paulter, "Carrier Lifetimes in Ion-Damaged GaAs," Applied Physics Letters, **54** (24), 2424 (1989).

27.   P. M. Downey, R. J. Martin, R. E. Nahory, and O. G. Lorimor, "High Speed, Ion Bombarded InGaAs Photoconductors," Applied Physics Letters, **46** (4), 396 (1985).

28.   A. Yariv, <u>Optical Electronics</u>, 4th Ed. (Saunders College Publishing, Philadelphia, PA, 1991, pp. 411-418).

29.   C.C. Hsu, B.P. McGinnis, J.P. Sokoloff, G. Khitrova, H.M. Gibbs, N. Peyghambarian, S.T. Johns and M.F. Krol, "Room-temperature optical nonlinearities of GaInAs/AlInAs and GaAlInAs/AlInAs multiple quantum wells and integrated-mirror etalons at 1.3 μm," submitted for publication.

MISSION

OF

ROME LABORATORY

Rome Laboratory plans and executes an interdisciplinary program in research, development, test, and technology transition in support of Air Force Command, Control, Communications and Intelligence (C^3I) activities for all Air Force platforms. It also executes selected acquisition programs in several areas of expertise. Technical and engineering support within areas of competence is provided to ESD Program Offices (POs) and other ESD elements to perform effective acquisition of C^3I systems. In addition, Rome Laboratory's technology supports other AFSC Product Divisions, the Air Force user community, and other DOD and non-DOD agencies. Rome Laboratory maintains technical competence and research programs in areas including, but not limited to, communications, command and control, battle management, intelligence information processing, computational sciences and software producibility, wide area surveillance/sensors, signal processing, solid state sciences, photonics, electromagnetic technology, superconductivity, and electronic reliability/maintainability and testability.